Analysis of Discrete Shallow-Water Models on Geodesic Delaunay Grids with C-Type Staggering

LUCA BONAVENTURA

Max-Planck-Institut für Meteorologie, Hamburg, Germany

TODD RINGLER

Department of Atmospheric Science, Colorado State University, Fort Collins, Colorado

(Manuscript received 4 May 2004, in final form 24 January 2005)

ABSTRACT

The properties of C-grid staggered spatial discretizations of the shallow-water equations on regular Delaunay triangulations on the sphere are analyzed. Mass-conserving schemes that also conserve either energy or potential enstrophy are derived, and their features are analogous to those of the C-grid staggered schemes on quadrilateral grids. Results of numerical tests carried out with explicit and semi-implicit time discretizations show that the potential-enstrophy-conserving scheme is able to reproduce correctly the main features of large-scale atmospheric motion and that power spectra for energy and potential enstrophy obtained in long model integrations display a qualitative behavior similar to that predicted by the decaying turbulence theory for the continuous system.

1. Introduction

Local wave propagation properties and global preservation of relevant flow invariants are usually considered to understand which discretization approach is most appropriate on a given grid. Representing accurately the basic solutions of the linearized equations of motion is essential to capture the key physical features of fluid motion and minimize the need for artificial numerical dissipation. Preservation of discrete equivalents of global invariants (such as mass, energy, potential vorticity, or potential enstrophy) guarantees that the approximation of the adiabatic and inviscid equations of motion does not induce trends in long-term integrations. A good choice for a discretization to be applied in a climate modeling GCM has to be satisfactory from both points of view.

For geophysical flows, the linear response of various possible staggered discretizations of the shallow-water equations was first analyzed in Winninghoff (1968) (see also Arakawa and Lamb 1977; Mesinger and Arakawa 1976). The general conclusion was that, at least for resolved Rossby radius, the C-type and B-type staggering according to the classification in Winninghoff (1968) displays the best wave dispersion behavior [see also the more recent analyses and comments in Dukowicz (1995) and Randall 1994)]. The C-grid staggering (discrete mass values computed at the center of the cell and discrete normal velocity components computed at the cell edges) also has the advantage that, in the incompressible limit, the marker-and-cell (MAC) approach of Harlow and Welch (1965) is recovered. Discretizations using staggered variable arrangements for incompressible fluids allow one to avoid spurious pressure modes (see, e.g., Quarteroni and Valli 1994) that arise in collocated grids (i.e., when all the discrete variables are assigned at the same discrete location). Spurious modes can be filtered by adding artificial numerical diffusion, but this implies that the accurately resolved scales are much larger than the nominal grid resolution. Thus, the C-grid arrangement yields a robust discretization technique that is appropriate for many of the flow regimes that are relevant for practical applications. This is important for models that should be applied efficiently also at very fine resolution.

The development of numerical methods combining good wave propagation with discrete conservation fea-

Corresponding author address: Luca Bonaventura, Max-Planck-Institut für Meteorologie, Bundesstraße 53, 20146, Hamburg, Germany.
E-mail: bonaventura@dkrz.de

tures appears thus highly desirable. Examples of methods using standard finite-differencing techniques on quadrilateral cells and possessing such properties are discussed in Arakawa and Lamb (1977, 1981), Janjic (1984), Mesinger and Arakawa (1976), Mesinger (1981), and Sadourny (1975). More recently, vorticity-preserving extensions of the Lax–Wendroff method for linear hyperbolic systems have been proposed in Morton and Roe (2001). The difficulties in satisfying both conservation of potential enstrophy and total energy on C grids have been clearly explained in Sadourny (1975). In that work, Sadourny discretized the nonlinear shallow-water equations on a plane using the C-grid staggering on a regular square grid. Depending upon how the velocity field and subsequent rotation term are reconstructed, Sadourny could obtain either potential enstrophy conservation or total energy conservation, but not both simultaneously. To obtain conservation of total energy, the rotation term had to be computed locally and then averaged to the adjacent velocity points. To obtain potential enstrophy conservation, the vorticity and velocities were averaged to the velocity point separately and the Coriolis force was then computed from the average quantities. In Arakawa and Lamb (1981), an energy- and potential-enstrophy-conserving scheme using the C grid was introduced. However, this was achieved at the cost of a rather unnatural representation of the Coriolis force and rotation terms in the momentum equation. More precisely, the extra degrees of freedom needed to satisfy both of the conservation constraints were introduced by letting, for example, the reconstruction of the velocity component v at the cell edge where u is defined depend also on the surrounding u velocity components. The resulting terms are differences in gridpoint values and should, for smooth flows, go to zero as the grid is refined. Energy- and potential-enstrophy-conserving schemes were derived for other types of staggering in Mesinger (1981) and Janjic (1984).

More recently, a new grid staggering, denoted by the authors as the Z/ZM grid arrangement, was introduced in Ringler and Randall (2002), using the hexagonal cells as control volumes. The ZM grid refers to the momentum form of the equations, where mass is defined at the centers of hexagons and full velocity vectors are defined at the corners of the hexagons. The Z grid, introduced in Randall (1994), refers to the vorticity-divergence form of the equations where mass, vorticity, and divergence are collocated at the centers of the hexagons. Using the mass and momentum equations, the authors construct a set of discrete operators that guarantees conservation of total energy. When the curl and divergence operators are applied to the momentum equation, the Z-grid equations are obtained and potential enstrophy conservation can then be guaranteed by the proper averaging of potential vorticity from cell centers to cell edges. The relationship between the Z grid and the approach proposed in Janjic (1984) has been highlighted in Gavrilov (2004).

The purpose of this paper is to understand how the known results for the quadrilateral C grid can be extended to discretizations of the shallow-water equations on quasi-uniform geodesic grids. Discretization grids obtained by inscription of the regular icosahedron in the sphere have been widely investigated since the early work of Arakawa, Sadourny, and Williamson around 1968 (Sadourny et al. 1968; Williamson 1968). They allow for quasi-uniform coverage of the sphere, thus solving automatically the pole problem and avoiding the high Courant numbers that arise when latitude–longitude grids are used. Furthermore, their hierarchical structure provides a very natural setting for multigrid and multiresolution approaches. A complete review of the earlier literature on this topic is given in Williamson (1979). More recently, the same type of grid has been employed in the development of new-generation GCMs at Colorado State University (see, e.g., Heikes and Randall 1995a; Ringler et al. 2000) and at the Frontier Research System for Global Change in Japan (see Tomita et al. 2001). Furthermore, the German Weather Forecast Service is using a hydrostatic model based on this grid for its operational global forecasting (see, e.g., Majewski et al. 2002). Other discretization approaches have also been proposed (see, e.g., Thuburn 1997; Stuhne and Peltier 1999; Giraldo 2000). Staggered grid discretizations on the icosahedral grid have been proposed by Sadourny as early as Sadourny (1969) and Sadourny and Morel (1969), although he did not investigate this approach further. S. Ničković analyzed the properties of C-grid staggering on hexagonal cells in Ničković (1994) and Ničković et al. (2002). These analyses have shown that computational, nonstationary geostrophic modes arise for basic second-order spatial discretization on plane, C-staggered hexagonal grids.

In this paper, we analyze numerical schemes for the shallow-water equations that use the analog of the C-grid staggering on triangular control volumes of regular Delaunay triangulations of the sphere. Geodesic icosahedral grids are a special case of such triangulations. Numerical schemes analogous to those derived by Sadourny (1975) are introduced, so that either potential enstrophy or energy conservation can be achieved. With the help of the results of Nicolaides

(1992), various properties of these schemes are also proved. Finally, it is shown by various numerical experiments that the potential-enstrophy-conserving scheme reproduces correctly the main features of large-scale atmospheric flows and could provide a sound basis for the development of numerical models for weather forecasting and climate simulation.

Here, as well as in Ringler and Randall (2002) and Thuburn (1997), the Voronoi–Delaunay property of the grid is exploited in an essential way. Although the icosahedral grid was used for the convenience of its grid-generation algorithm, the results presented here apply to generic Delaunay triangulations of the sphere, under mild regularity assumptions (see, e.g., Nicolaides 1992). The use of triangular control volumes is currently being envisaged within the icosahedral nonhydrostatic (ICON) dynamical core project [see Bonaventura (2003) for a description of the project and of its preliminary results]. The use of triangular cells as control volumes is appealing because it allows for easier development of mass-conserving local refinement approaches, along the lines of the Cartesian mesh refinement approaches (see, e.g., Berger and Colella 1989; Leveque 1996; Almgren et al. 1998; Bonaventura and Rosatti 2002). Numerical methods based on triangular Delaunay C grids for realistic high-resolution simulations in estuarine dynamics have been introduced in Casulli and Zanolli (1998) and Casulli and Walters (2000).

In section 2, the shallow-water equations will be briefly reviewed. The grid-generation process and the C-grid variable arrangement are discussed in section 3. In section 4, discrete operators are introduced and are shown to have a number of mimetic properties, that is, discrete analogs of basic formulas that hold for continuous functions. Since in a C-grid discretization components of the velocity vector normal to the cell edges are computed at different points, algorithms to reconstruct a full velocity vector from these components are discussed in section 5. The spatial discretization of the shallow-water equations is then introduced in section 6, along with an analysis of its main features. Details of the proofs are given in appendixes A and B for the potential-enstrophy-preserving and the energy-preserving variant, respectively. A semi-implicit time discretization is then introduced in section 7, based on the predictor-corrector approach proposed in Lin and Rood (1997). Results obtained with this discretization on some of idealized test cases are presented in section 8. Results obtained with an explicit Adams–Bashforth discretization are also shown, for the sake of clear comparison with the findings in Ringler and Randall (2002).

2. The shallow-water equations

The shallow-water equations are written here in vector invariant form and with the same notation used in Ringler and Randall (2002):

$$\frac{\partial h}{\partial t} + \nabla \cdot (\mathbf{v}h) = 0, \tag{1}$$

$$\frac{\partial \mathbf{v}}{\partial t} = -\eta \mathbf{k} \times \mathbf{v} - \nabla[g(h + h^s) + K], \tag{2}$$

where $\mathbf{v}$ is the velocity vector, $\eta = \zeta + f$ is the absolute vorticity, ζ is the vertical component of the relative vorticity, h fluid depth, h^s is orographic height, and K the kinetic energy per unit mass $K = |\mathbf{v}|^2/2$. The potential vorticity can be defined in this context as $q = \eta/h$, so that potential enstrophy is given by q^2. Potential vorticity and potential enstrophy are conserved quantities and obey the same conservation law of generic passive tracers with concentration c,

$$\frac{\partial (ch)}{\partial t} + \nabla \cdot (\mathbf{v}ch) = 0. \tag{3}$$

The need to employ consistent discretizations of Eqs. (1) and (3) has been stressed already in Arakawa and Lamb (1981), Schär and Smolarkiewicz (1996), and highlighted recently in Gross et al. (2002), Jöckel et al. (2001), and Ringler and Randall (2002).

3. The icosahedral grid and the C-type staggering

The construction process of the icosahedral geodesic grid is described in Baumgardner and Frederickson (1985). The regular icosahedron is inscribed in the sphere, so as to obtain 20 spherical triangles. The sides of these triangles are then bisected, thus producing four smaller triangles for each original triangle. This procedure can be repeated an arbitrary number of times, so as to achieve triangulations with the desired resolution. These triangulations are in fact *Delaunay* triangulations; that is, none of the triangle vertices lies inside the circumcircle of any triangle. A *Voronoi* tessellation is naturally associated to each Delaunay triangulation (see, e.g., Augenbaum and Peskin 1985; Rebay 1993; Quiang et al. 2003). A Voronoi cell is the set of all points on the sphere closer to a vertex of a Delaunay triangulation than to any other point. Given a Delaunay triangulation, these Voronoi cells cover the whole sphere without overlapping and consist of convex spherical polygons. In the case of the triangulation obtained from the refinement of the icosahedron, these Voronoi cells are either pentagons or hexagons (see Fig. 1). It can be proven (see, e.g., the references in

FIG. 1. Delaunay (triangular) and Voronoi (hexagonal–pentagonal) icosahedral grid at the first grid-refinement level.

TABLE 1. List of symbols used for the description of the grid.

Symbol	Grid quantity
i	Center of Delaunay grid cell
v	Center of Voronoi grid cell (vertex of Delaunay grid cell)
l	Delaunay or Voronoi grid edge
$\mathcal{E}(i)$	Edges of cell i
$\mathcal{C}(v)$	Cells of which v is a vertex
$\mathcal{E}(v)$	Edges of dual cell v
$\mathcal{E}(l)$	Edges of Voronoi grid attached to edge l
A_i	Area of cell i
A_v	Area of dual cell v
λ_l	Length of the primal cell edge l
δ_l	Length of the dual cell edge l
$\mathbf{N}_l$	Unit vector normal to the primal grid edge l
$\mathbf{T}_l$	Unit vector tangential to the primal grid edge l
$\mathbf{n}_{i,l}$	Outer normal unit vector at edge primal cell i
$\mathbf{t}_{v,l}$	Outer normal unit vector at edge dual cell v
$i(l, 1)$, $i(l, 2)$	Primal cells adjacent to edge l
$v(l, 1)$, $v(l, 2)$	Dual cells adjacent to edge l

Hermeline 1993) that for each side of a Voronoi cell there is a unique orthogonal side of a Delaunay triangle associated to it. It should be remarked that, although we will only refer for concreteness to the icosahedral grid, all the properties of the numerical scheme derived in the following will hold also for more general Voronoi–Delaunay pairs on the sphere, provided that some basic regularity requirements are satisfied (see, e.g., Nicolaides 1992).

Some notation to describe the grid topology and geometry will now be introduced. A list of the main symbols used in the following is provided for reference in Table 1. It is to be remarked that, in principle, the roles of the Voronoi and the Delaunay grid are perfectly symmetric, so that either of them can be assumed as primal grid. However, for reasons to be explained more fully later, in the numerical methods that will be introduced here the Delaunay grid will be used as primal grid. Let then i denote the generic triangular cell of the Delaunay grid. Let $\mathcal{E}(i)$ denote the set of all edges of cell i, and $\mathcal{C}(i)$ denote the set of all cells that have edges in common with cell i. The grid point associated to cell i will also be referred to as the cell center. The generic vertex of a cell, which is also the center of a (hexagonal or pentagonal) cell in the dual grid, is denoted by v. Here $\mathcal{C}(v)$ denotes the set of all cells of which v is a vertex, and $\mathcal{E}(v)$ denotes the set of all edges of the dual cell whose center is vertex v. The area of cell i is denoted by A_i, while the area of the dual cell is denoted by A_v. Let then l denote the generic edge of a cell. It is to be remarked that this index can be assigned at the same time to an edge of the primal grid and the edge of the dual grid, which by construction intersects the primal grid edge at its midpoint. The number of edges is actually equal for both grids. Let $\mathcal{E}(l)$ denote the set of four edges of the dual Voronoi grid attached to edge l. The length of the edge l of a cell is denoted by λ_l, and the distance between the centers of the cells adjacent to edge l (i.e., the length of a edge of the dual cell) is denoted by δ_l. At each edge, a unit vector $\mathbf{N}_l$ normal to the edge l is assigned; $\mathbf{T}_l$ denotes the unit vector tangential to the edge l, chosen in such a way that $\mathbf{N}_l \times \mathbf{T}_l = \mathbf{k}_l$ holds. Here and in the following, $\mathbf{k}_l$ will denote the radial outgoing unit vector perpendicular to the tangent plane at the velocity point on edge l. Furthermore, for each cell edge, the unit vector pointing in the outer normal direction with respect to cell i is denoted by $\mathbf{n}_{i,l}$. Unit vectors $\mathbf{n}_{v,l}$ are also introduced, as pointing in the outer normal direction with respect to the dual cell v. The corresponding tangential vectors $\mathbf{t}_{v,l}$ are defined so that $\mathbf{n}_{v,l} \times \mathbf{t}_{v,l} = \mathbf{k}_l$. It can be seen that, by simple geometric arguments, one has $\mathbf{N}_l \cdot \mathbf{t}_{v,l} = -\mathbf{T}_l \cdot \mathbf{n}_{v,l}$.

To develop an analog of the C-type staggering on the Voronoi or Delaunay grids, the *mass points* are defined as the centers of the grid cells, while the *velocity points* are defined for each cell edge as the intersection between the edges of the Voronoi and Delaunay cells (see Fig. 2). By construction, each of these points is the midpoint of an edge of a Delaunay cell and equidistant from the centers of the Voronoi cells at the ends of that edge. A velocity point is also the intersection of the edge of the cell with the arc connecting the centers of the cells adjacent to that edge. These points are the

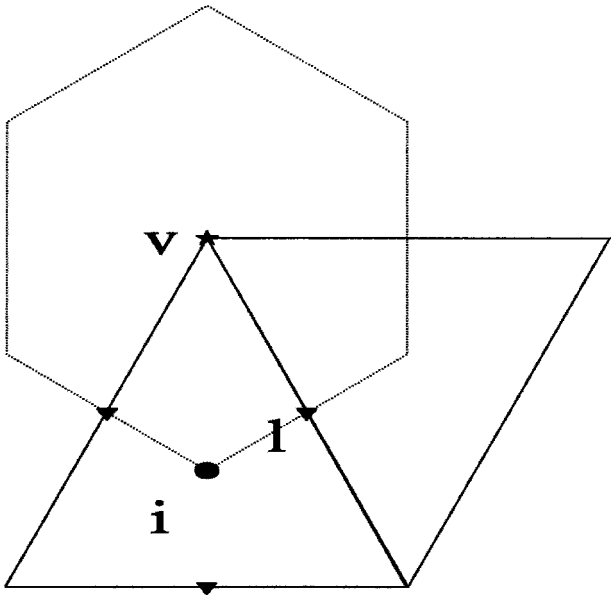

FIG. 2. Primal and dual cells in C-grid staggering on the triangular icosahedral grid.

locations of the discrete normal velocity components with respect to the cell edge. It should be observed that the velocity points are not equidistant from the adjacent Delaunay grid cell centers. However, grid optimization procedures such as those introduced in Heikes and Randall (1995b) can partly cure this problem, as shown in Table 2, by reducing to rather small values the off-centering of the velocity point with respect to the neighboring mass points. Given the edge l of a cell, the adjacent cells are denoted by the indexes $i(l, 1)$ and $i(l, 2)$, respectively. The indices are chosen so that the direction from $i(l, 1)$ to $i(l, 2)$ is the positive direction of the normal vector $\mathbf{N}_l$. Vertex indexes $v(l, 1)$ and $v(l, 2)$ can also be defined analogously, so that the direction from $v(l, 1)$ to $v(l, 2)$ is the positive direction of the vector $\mathbf{T}_l$. Given a generic discrete vector field $\mathbf{g}$ on the sphere, its value at a velocity point can be represented as $\mathbf{g}_l = g_l\mathbf{N}_l + \hat{g}_l\mathbf{T}_l$, where g_l, $\hat{g}_l$ denote the normal and the tangential components, respectively.

TABLE 2. Quasi uniformity of the triangular icosahedral grids after Heikes–Randall optimization.

Level	$A_{\min}/A_{\max}$	$\lambda_{\min}/\lambda_{\max}$	Velocity point off-centering (%)
0	1	1	0.0
1	0.83	0.88	19.9
2	0.89	0.80	12.0
3	0.92	0.78	6.5
4	0.93	0.78	3.4
5	0.94	0.78	1.7
6	0.94	0.78	0.97

In a C-grid discretization approach, the discrete prognostic variables considered are the value of the height field h_i at the mass points (interpreted as a cell-averaged value) and the normal velocity components u_l. The tangential velocity components, which are needed, for example, for the computation of the Coriolis force term, must be reconstructed. Furthermore, the value of kinetic energy (K) at the mass points has to be defined, in order for a discretization of Eq. (2) to be feasible. Finally, averaged values $\overline{h}_l$, $\overline{\eta}_l$, and $\overline{c}_l$ have to be introduced for the computation of the mass, potential vorticity, and tracer fluxes. The specific way in which this averaging can be performed will be discussed later.

4. Discrete operators and discrete Helmholtz decomposition

Discrete divergence and curl operators are now introduced in the context of the C-grid staggering outlined above. These operators are defined as acting on a set of values g_l assigned at the edges of the Voronoi–Delaunay grid. These are to be interpreted as the components of a vector field $\mathbf{g}_l$ normal to the cell edges, that is, $g_l = \mathbf{g}_l \cdot \mathbf{N}_l$. The discrete divergence and curl operator can be naturally defined as follows:

$$\mathrm{div}(g)_i = \frac{1}{A_i} \sum_{l \in \mathcal{E}(i)} g_l \mathbf{N}_l \cdot \mathbf{n}_{i,l} \lambda_l, \tag{4}$$

$$\mathrm{curl}(g)_v = \frac{1}{A_v} \sum_{l \in \mathcal{E}(v)} g_l \mathbf{N}_l \cdot \mathbf{t}_{v,l} \delta_l. \tag{5}$$

It is to be observed that the divergence operator is defined on the primal grid (i.e., at the cell centers), while the curl operator is defined on the dual grid (i.e., at the cell vertices). Analogous operators can be defined on the dual grid. In the following, only the discrete divergence operator on the dual grid cells will be used, which can be defined as

$$\mathrm{div}(g)_v = \frac{1}{A_v} \sum_{l \in \mathcal{E}(v)} g_l \mathbf{T}_l \cdot \mathbf{n}_{v,l} \delta_l, \tag{6}$$

which is simply a restatement of definition 4 on the dual grid. By straightforward application of Green and Stokes theorems, it can be shown that these definitions yield consistent approximations of the corresponding differential operators. The Voronoi–Delaunay property of the grid (the normal direction to the edges of the primal grid cell is the tangential direction to the corresponding edge of the dual grid cell) has been used here in an essential way. By the same property, the discrete normal and tangential derivatives can also be approximated as

$$\delta_\nu \phi_l = \frac{\phi_{i(l,2)} - \phi_{i(l,1)}}{\delta_l}, \tag{7}$$

$$\delta_\tau \psi_l = \frac{\psi_{\upsilon(l,2)} - \psi_{\upsilon(l,1)}}{\lambda_l}, \tag{8}$$

where ϕ_i, ψ_υ are discrete functions defined on the primal and dual grid cells, respectively.

These discrete operators have properties similar to those of their continuous counterparts. Consider, for example, the formula for integration by parts on the sphere

$$\int_S \phi \, \mathrm{div}(\mathbf{g}) \, d\sigma = -\int_S \nabla\phi \cdot \mathbf{g} \, d\sigma . \tag{9}$$

The discrete equivalent of the surface integral on the left-hand side can be reformulated as

$$\sum_i A_i \phi_i \, \mathrm{div}(g)_i = \sum_i \phi_i \sum_{l \in \mathcal{E}(i)} g_l \mathbf{N}_l \cdot \mathbf{n}_{i,l} \lambda_l \tag{10}$$

by means of definition (4). The sum on the right-hand side can then be rearranged as a sum over all cell edges, considering that, when summing over all the cell centers as in Eq. (10), each edge is actually counted twice (once for each cell adjacent to that edge), so as to obtain

$$\sum_i \phi_i \sum_{l \in \mathcal{E}(i)} g_l N_l \cdot n_{i,l} \lambda_l = \sum_l g_l \lambda_l [\phi_{i(l,1)} \mathbf{N}_l \cdot \mathbf{n}_{i(l,1),l} + \phi_{i(l,2)} \mathbf{N}_l \cdot \mathbf{n}_{i(l,2),l}]. \tag{11}$$

If the term in square brackets is multiplied and divided by δ_l and the definitions in section (3) are used, this yields finally the discrete equivalent of Eq. (9):

$$\sum_i A_i \phi_i \, \mathrm{div}(g)_i = -\sum_l \delta_\nu \phi_l g_l \lambda_l \delta_l. \tag{12}$$

Furthermore, a discrete analog of the Helmholtz decomposition theorem can be proven, which will be used to analyze the discretization of the shallow-water equations in the following section. The Helmholtz [or Helmholtz–Hodge decomposition (see, e.g., Chorin and Marsden 1993)] is an essential tool in theoretical analyses of fluid flow. For example, potential flow theory relies heavily on it, as well as existence and uniqueness proofs for the two dimensional Navier–Stokes equations [see, e.g., the review in Girault and Raviart (1986)]. The discrete version of the Helmholtz decomposition allows one, then, to achieve discrete analogs of many of these results. The proof of the discrete Helmholtz decomposition goes along the same lines as the results proven in Nicolaides (1992) for Voronoi–Delaunay grids on the plane. The only modification required is in the proof of theorems 4.1 and 4.2 of Nicolaides (1992), where it has to be taken into account that the Euler characteristic of the sphere is 2 (see, e.g., Massey 1977), that is, $E + 2 = N + T$, where E is the number of edges, T the number of the primal (triangular) cells, and N the number of dual cells. Given discrete values g_l for each edge of the grid, the relevant properties of the discrete operators can be summarized as follows:

Lemma 1: $\mathrm{div}(g)_i = 0$ for all cells i if and only if there exist ψ_υ such that $g_l = \delta_\tau \psi_l$.

Lemma 2: $\mathrm{curl}(g)_\upsilon = 0$ for all dual cells υ if and only if there exist ϕ_i such that $g_l = \delta_\nu \phi_l$.

Theorem 1: For any g, there exist g_l^d and g_l^r such that $g_l = g_l^d + g_l^r$, $\Sigma_l \, g_l^d g_l^r \lambda_l \delta_l = 0$, and $\mathrm{div}(g^r)_i = 0$, $\mathrm{curl}(g^d)_\upsilon = 0$, respectively.

Theorem 2: Given discrete values ρ_i, ω_υ, there exists a unique set of discrete values g_l such that $\mathrm{div}(g)_i = \rho_i$ and $\mathrm{curl}(g)_\upsilon = \omega_\upsilon$ for all primal and dual cells, respectively.

This result relies essentially on the fact that the discrete global integral of ρ_i and ω_υ is zero, just as in the continuous case; see, for example, Eq. (12). These properties will be used in the analysis of the spatial discretization given in section 6. Taken together, theorem 1 and theorem 2 guarantee that, even at the discrete level, the velocity field and the vorticity-divergence fields are interchangeable. All of the information present in the velocity field can be recovered from the vorticity-divergence fields, and vice versa. At a conceptual level this is critical because it means that a theorem that exists for the continuous system, the Helmholtz decomposition, can be used without loss of generality in the discrete system.

5. Reconstruction of a vector field from the normal components

To recover the full velocity vector from the normal velocity components prescribed at the velocity points in a C-grid variable staggering, a reconstruction procedure is needed. This is essential for the discretization of the shallow-water equations, especially for the representation of the Coriolis force terms. If the control volumes are triangular, standard algorithms for the vector reconstruction are available from the finite-volume or finite-element literature. We will always be concerned here with a vector field $\mathbf{g}$, whose normal components g_l are assumed to be known at the edges of a plane Delaunay triangulation. In Nicolaides (1992) a cellwise constant, first-order-accurate reconstruction algorithm for the vector field $\mathbf{g}$ has been introduced. It was also proven that, if the discrete set of values g_l is such that

$\mathrm{div}(g)_i = 0$ for all cells i, this is the unique piecewise constant reconstruction that yields back the g_l as the normal components. Once the vector $\mathbf{g}$ has been reconstructed at the cell center, the value of the tangential vector component at the velocity point can be obtained by averaging the vectors of the neighboring cells and projecting in the direction tangential to the cell edge. For example, the convergence proofs of Nicolaides (1992) hold for the tangential component reconstruction given by the formula

$$\hat{g}_l = \sum_{l' \in \mathcal{E}(l)} g_{l'} \alpha_{l,l'} w_{l,l'}, \tag{13}$$

where $w_{l,l'} = \mathbf{T}_l \cdot \mathbf{N}_{l'}$ and $\alpha_{l,l'}$ are appropriate weighting coefficients such that $\alpha_{l,l'} = \alpha_{l',l}$. It can be observed that, by simple geometric arguments, $w_{l,l'} = -w_{l',l}$.

Alternatively, the cellwise linear reconstruction introduced in Raviart and Thomas (1977) in the context of hybrid finite-element methods on the plane can be used. A complete description of the mathematical properties of this reconstruction is given, for example, in Quarteroni and Valli (1994). This reconstruction, also known as the Raviart–Thomas element of order 0 (RT0) in the finite-element literature, yields for each cell i a uniquely defined linear function $\mathbf{g}_i(\mathbf{x})$ that gives back the g_l as normal components when evaluated at the velocity points. Furthermore, the normal components are continuous along the cell boundaries, the piecewise linear reconstruction is irrotational within each cell, and the divergence of the reconstructed field $\mathbf{g}_i$ is a constant that is equal to the discrete divergence $\mathrm{div}(g)_i$ computed from the field's discrete normal components. It is to be remarked that this is the unique reconstruction with these properties and that it is completely identified by the specification of the normal components. However, the tangential velocity components are in general discontinuous. Once the vector field has been reconstructed within each cell, the value of the tangential vector component at the velocity point can obtained by averaging onto the edge the adjacent reconstructed vectors and projecting in the direction tangential to the cell edge.

It is at this stage that one of the differences arises between the C-grid staggering on the Delaunay (triangular) and Voronoi (pentagonal/hexagonal) icosahedral grids (see also the discussion at the end of section 6). The reconstruction of a single velocity vector on the hexagonal grid is far less straightforward. It can be shown with arguments along the lines of Nicolaides (1992) that there is, in general, no uniquely determined piecewise constant reconstruction on a hexagonal grid, even in the divergence-free case. To these authors' knowledge, no standard result is available from finite-element theory either.

6. The spatial discretization of the shallow-water equations and their properties

Given the spatial discretization operators introduced above, Eqs. (1)–(2) can be discretized as follows on the triangular Delaunay grid. Assuming that $\mathbf{v} = u_l \mathbf{N}_l + v_l \mathbf{T}_l$, the space discretization of the continuity equation is given by

$$\frac{\partial h_i}{\partial t} = -\mathrm{div}(\overline{h}u)_i, \tag{14}$$

where $\overline{h}_l$ is an average of height values at the cell edge. It will be seen in the following that the properties of the resulting scheme do not depend on the choice of this averaging method for the discrete mass variables. The discrete momentum equation can be derived by taking the scalar product of Eq. (2) with the unit vector $\mathbf{N}_l$ at a generic velocity point. Using the vector identity

$$(\mathbf{k}_l \times \mathbf{v}) \cdot \mathbf{N}_l = -\mathbf{v} \cdot (\mathbf{k}_l \times \mathbf{N}_l)$$

and the definitions given in the previous section yields the equation

$$\frac{\partial u_l}{\partial t} = \overline{\eta}_l v_l - \delta_v [g(h + h^s) + K]_l. \tag{15}$$

Here, $\eta_v = \zeta_v + f_v$, where $\zeta_v = \mathrm{curl}(u)_v$, and $\overline{\eta}_l$ is an average of the absolute vorticity values at the cell edge to be specified later. The discrete tracer equation consistent with Eq. (14) is given by

$$\frac{\partial (ch)}{\partial t} = -\mathrm{div}(\overline{c}\overline{h}u)_i, \tag{16}$$

where $\overline{c}_l$ denotes some averaged value of the tracer concentration at the cell edge. It is to be remarked that a specific choice for the averaging method determines a specific advection scheme that is consistent with the discrete continuity Eq. (14) by construction. It was shown in Schär and Smolarkiewicz (1996), Liu (1993), and Gross et al. (2002) that this property is essential for the effective monotonicity of an advection scheme. For example, preservation of initially constant fields cannot be granted without this property.

An important feature of this type of spatial discretizations is that, as in the continuous case, taking the discrete curl of the momentum equation yields automatically a consistent discretization of the relative vorticity equation. This can be shown using the equality $\mathbf{N}_l \cdot \mathbf{t}_{v,l} = -\mathbf{T}_l \cdot \mathbf{n}_{v,l}$ (see section 3) and the properties of

the discrete operators reviewed before. Taking the time derivative of the discrete vorticity one obtains

$$\frac{\partial \zeta_v}{\partial t} = \frac{1}{A_v} \sum_{l \in \mathcal{E}(v)} \frac{\partial u_l}{\partial t} \mathbf{N}_l \cdot \mathbf{t}_{v,l} \delta_l,$$

$$= \frac{1}{A_v} \sum_{l \in \mathcal{E}(v)} [\overline{\eta}_l v_l - \delta_v (g(h + h^s) + K)_l] \mathbf{N}_l \cdot \mathbf{t}_{v,l} \delta_l,$$

$$= \frac{1}{A_v} \sum_{l \in \mathcal{E}(v)} \overline{\eta}_l v_l \mathbf{N}_l \cdot \mathbf{t}_{v,l} \delta_l = -\mathrm{div}(\overline{\eta} v)_v. \tag{17}$$

Here, the fact that $\mathrm{curl}(\delta_v \phi_l) = 0$ for any ϕ_i has been used. Therefore, the spatial discretization of the momentum equation leads to a vorticity production that corresponds exactly to that implied by the discretization of the equations of motion in vorticity–divergence form. The advantages of this property for finite-difference discretizations were highlighted, for example, in Lin and Rood (1997). It is to be stressed that the same result can be achieved on any dual Voronoi–Delaunay pair. Staggered grid discretizations on quadrilateral grids also displaying this property have been introduced in Sadourny (1975) and Lin and Rood (1997).

The value of the tangential velocity component v_l used in Eqs. (15) and (17) is obtained from the normal components u_l by one of the reconstruction algorithms discussed in section 5. Assume now that the velocity reconstruction algorithm and the averaging rule for the computation of $\overline{h}_l$ have been specified. In implementation used for the numerical tests, simple arithmetic averaging was used to compute $\overline{h}_l$, while the Raviart–Thomas algorithm described in section 5 was used for the velocity field. The mass fluxes through the edges of the dual cells are then uniquely defined. As a consequence, a spatially discrete continuity equation on the dual cells, which is consistent with (15) and (17), can be uniquely defined as

$$\frac{\partial h_v}{\partial t} = -\mathrm{div}(\overline{h} v)_v. \tag{18}$$

It is to be remarked that this equation is not obtained as an average of the mass equations on the triangular cells, but rather defines the only way to compute the tendency $(\partial h_v/\partial t)$ that is consistent with the vorticity fluxes defined by (17). The values h_v are to be understood as completely determined by the time evolution imposed by (18), once their initial values have been assigned, for example, by area weighted averaging. If the edge-averaged potential vorticity values are defined as $\overline{q}_l = \overline{\eta}_l/\overline{h}_l$, Eq. (17) implies then

$$\frac{\partial (q_v h_v)}{\partial t} = -\mathrm{div}(\overline{q}\overline{h} v)_v, \tag{19}$$

thus showing that the proposed spatial discretization conserves potential vorticity.

Conservation of potential enstrophy can then be obtained by combining appropriately Eqs. (19) and (18). In this way, the analog of the potential-enstrophy-preserving scheme obtained in Sadourny (1975) is derived for C-type staggering on spherical Delaunay triangulations. The complete derivation of the potential-enstrophy-conserving scheme is reported in appendix A and is achieved by arguments similar to those in Sadourny (1975), Arakawa and Lamb (1977), and Ringler and Randall (2002). It is shown in appendix A that potential enstrophy conservation will hold if the edge-averaged value of potential vorticity is obtained by simple arithmetic average, which entails

$$\overline{\eta}_l = \frac{\overline{h}_l}{2} \left[\frac{\eta_v(l, 1)}{h_v(l, 1)} + \frac{\eta_v(l, 2)}{h_v(l, 2)} \right]. \tag{20}$$

It is to be remarked, however, that the potential enstrophy spectra obtained with this type of averaging were almost identical to those obtained employing, for example, simple arithmetic average of the values of η_v at the neighboring vertices (see section 8). It was more straightforward to employ this simpler formulation in the two-time-level semi-implicit scheme described in section 7. However, the formulation of (20) could be easily incorporated in a three-time-level semi-implicit scheme and was used together with an explicit time discretization in some of the tests discussed in section 8.

The spatial discretization given by Eqs. (14)–(19) does not in general conserve energy as well. Let the discrete kinetic energy be defined as

$$K_i = \frac{1}{2} \sum_{l \in \mathcal{E}(i)} R_{i,l} u_l^2, \tag{21}$$

where $R_{i,l}$ are weighting coefficients to be defined later. The total energy is then defined as

$$E = \sum_i A_i h_i \left[g\left(\frac{h_i}{2} + h_i^s \right) + K_i \right]. \tag{22}$$

It will be shown in appendix B that, in the absence of rotation, E is constant for flows such that $\mathrm{curl}(u)_v = 0$. It will also be shown how the discretization of the rotation term in the previous scheme can be modified along the lines of Arakawa and Lamb (1981), so as to obtain an energy-conserving scheme. This alternative scheme does not, in general, conserve potential enstrophy. The relative merits of potential enstrophy versus energy-conserving schemes on C-type staggered grids were analyzed by Sadourny in Sadourny (1975) on the basis of two-dimensional turbulence theory. His con-

clusion was that ". . . Conservation of potential enstrophy in the nonlinear interactions involving triads of internal wavenumbers is thus an essential requirement for long term numerical integrations." In the present paper, only numerical results obtained with the potential-enstrophy-conserving scheme will be presented.

Other important properties of this type of discretization can be highlighted by considering its application to the linear shallow-water equations, along the lines of the analysis carried out in Le Roux et al. (1998) and in the literature reviewed therein. Linearizing Eqs. (1)–(2) around a steady state with reference height H and no orography and applying the spatial discretization described above yields

$$\frac{\partial h_i}{\partial t} = -H \operatorname{div}(u)_i, \tag{23}$$

$$\frac{\partial u_l}{\partial t} = f_l v_l - g\delta_v h_l. \tag{24}$$

If stationary solutions are sought and the Coriolis force is neglected, one obtains the discrete equations

$$\operatorname{div}(u)_i = 0, \quad \delta_v h_l = 0. \tag{25}$$

Since the only solutions to $\delta_v h_l = 0$ are constants, there are no spurious pressure modes for this type of discretization. Furthermore, if vorticity values ζ_v are prescribed, by the discrete Helmholtz decomposition theorem there exists a unique discrete field u_l such that $\operatorname{curl}(u)_v = \zeta_v$ and $\operatorname{div}(u)_i = 0$. Thus, if Eqs. (23)–(24) are initialized with discrete fields that satisfy conditions (25), in the absence of rotation the stationary solution will be maintained. If Eqs. (23)–(24) are considered on an f plane with constant Coriolis force and, again, stationary solutions are sought, the discrete velocity field is also uniquely determined by the specification of the discrete vorticity and the height can be recovered up to a constant from equation $fv_l = g\delta_v h_l$.

In the absence of rotation, all these results hold for either the Delaunay or the dual Voronoi grid. In the general case, the only points in which the C-grid discretizations on these two grids differ are the reconstruction procedure for the tangential velocity field (see the discussion in section 5) and the fact that spurious vorticity modes can arise for the C-grid arrangements on the hexagonal grid. This can be shown by considering that, on the dual grid, the mass points would be the hexagon centers and vorticity would be computed at the centers of the triangular cells. However, a uniform equilateral tessellation allows for a checkerboard pattern (see, e.g., Fig. 3). In case such a pattern were developed for any reason in the vorticity field, simple averaging of such vorticity values onto the hexagon edge would result in a null contribution to the nonlinear rotation term. Thus, the dynamics of such modes would be completely decoupled, possibly leading to amplification of numerical errors. On the other hand, no checkerboard mode is possible on the hexagonal grid. The divergence, which is naturally computed on the triangles of the Delaunay C grid, and may thus develop similar spurious modes, is never averaged in standard discretization approaches. Furthermore, divergence damping can be used, if necessary, to control any noise in the divergence field. Although these considerations only hold rigorously for equilateral tessellations, they can be regarded as an indication of potential problems on the nonuniform grids on the sphere.

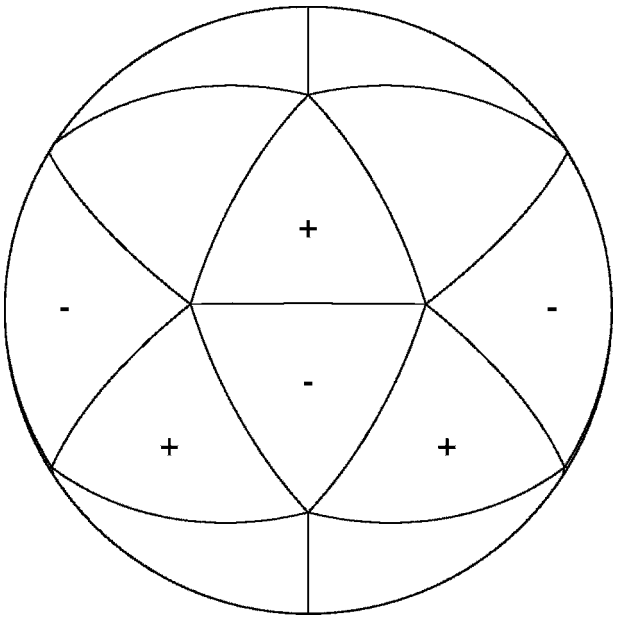

FIG. 3. Spurious vorticity mode on the dual triangular grid for hexagonal C-grid arrangement.

7. A semi-implicit time discretization

The semi-implicit time discretization already introduced in Bonaventura (2003) will be described, which will then be used to perform various numerical experiments that are fully described in section 8. It is meant to be only an example of a feasible approach for the time discretization of Eqs. (14)–(15). Other possible approaches, such as, for example, three-time-level semi-implicit discretization using leapfrog time stepping, are currently being considered.

The proposed discretization consists of a simple two-time-level scheme based on the trapezoidal integration rule, which is given by

TABLE 3. Relative errors and convergence rates in shallow-water test case 3.

Level	l_1 error	l_1 rate	l_2 error	l_2 rate	l_∞ error	l_∞ rate
3	3.6×10^{-2}	—	4.6×10^{-2}	—	0.1	—
4	8.6×10^{-3}	2.06	1.3×10^{-2}	1.85	4.0×10^{-2}	1.43
5	2.9×10^{-3}	1.57	4.6×10^{-3}	1.49	1.6×10^{-2}	1.36
6	8.5×10^{-4}	1.76	1.4×10^{-3}	1.72	5.3×10^{-3}	1.58
7	2.4×10^{-4}	1.82	4.1×10^{-4}	1.77	1.6×10^{-3}	1.73

$$u_l^{n+1} = u_l^n + \Delta t \tilde{\bar{\eta}}_l^{n+\alpha} v_l^{n+\alpha} - \Delta t\{\delta_\nu[g(h^{n+\alpha} + h^s) + \tilde{K}^{n+\alpha}]\}_l, \quad (26)$$

$$h_i^{n+1} = h_i^n - \Delta t \, \mathrm{div}(\bar{h}^n u^{n+\alpha})_i. \quad (27)$$

Here, $\phi^{n+\alpha} = \alpha\phi^{n+1} + (1 - \alpha)\phi^n$, and $\alpha \in [\frac{1}{2}, 1]$ for stability, with $\alpha = \frac{1}{2}$ yielding a second-order-accurate time discretization in the linear case. As it is well known, off-centering of the time discretization by taking values larger than $\frac{1}{2}$ adds implicit numerical diffusion. Values in the range [0.6, 0.7] are quite common for models using two-time-level semi-implicit discretizations. Here $\tilde{\psi}^{n+\alpha}$ denotes instead an approximation of the value of ψ at time $(n + \alpha)\Delta t$ obtained by an explicit discretization. In particular, the intermediate update of η is computed by a time discretization of Eq. (17). The specific type of explicit update employed is crucial for the accuracy of the resulting numerical scheme. In the implementations tested in section 8, only simple upwind schemes were employed for this update. Further-

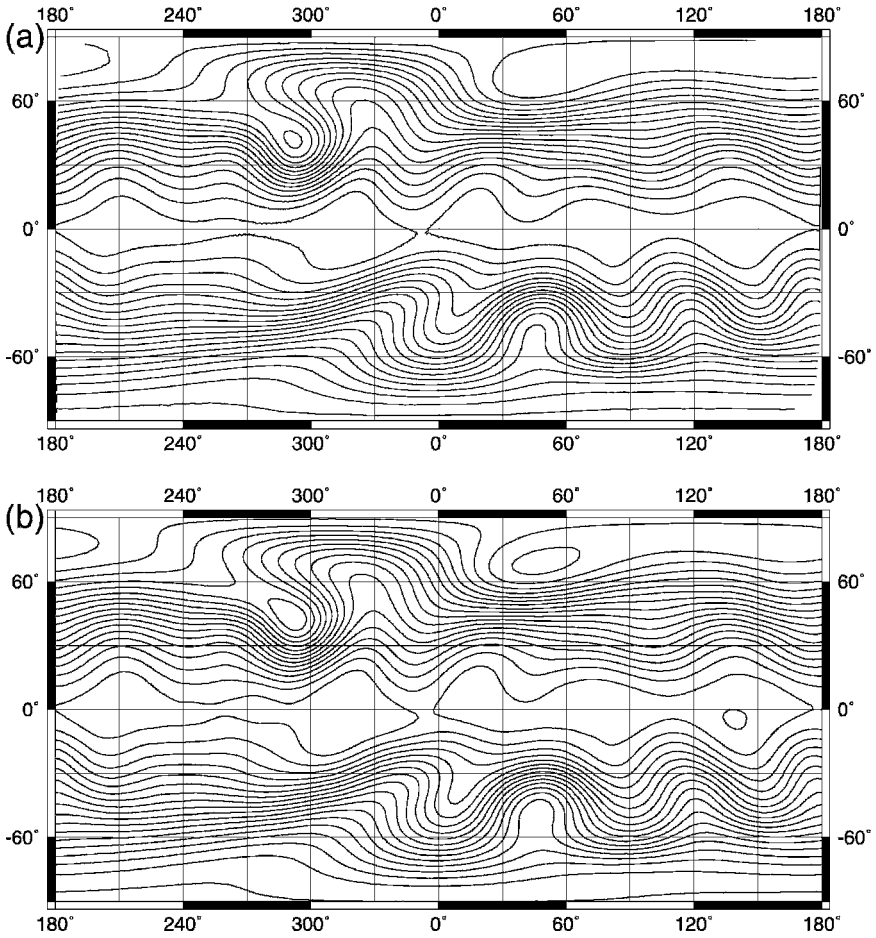

FIG. 4. Geopotential height at day 15 in test case 5, as computed (a) by the C-grid shallow-water model and (b) by the NCAR reference spectral model at T106. Contour line spacing is 50 m.

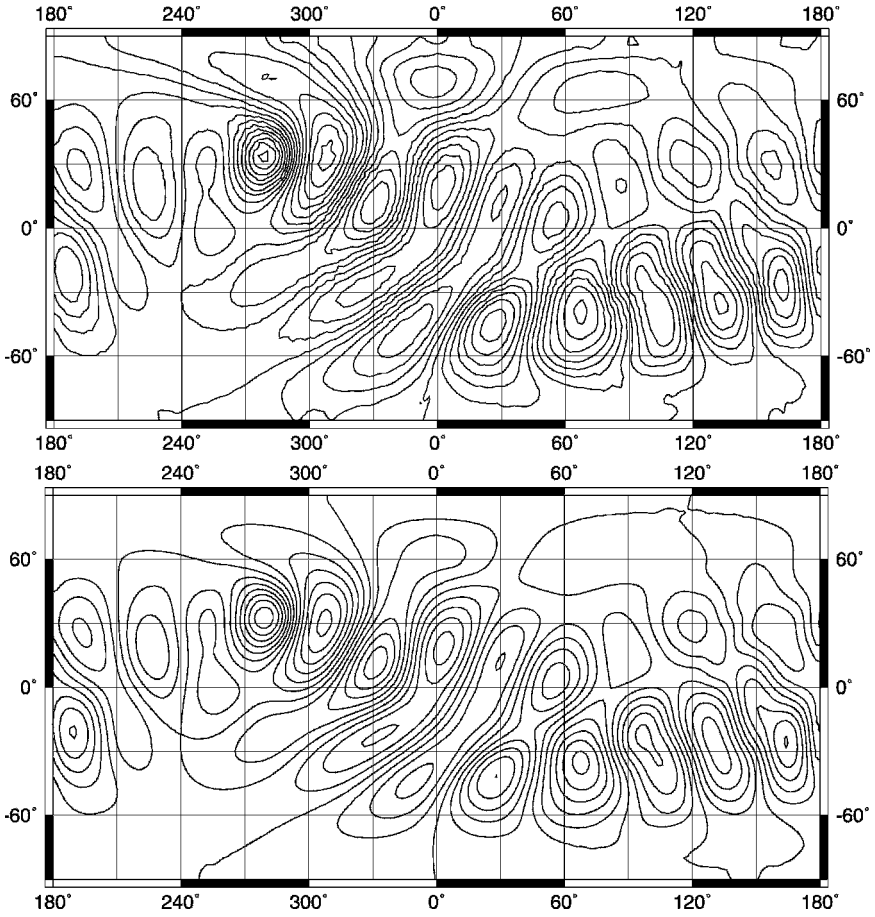

FIG. 5. Meridional velocity at day 15 in test case 5, as computed by (a) the C-grid shallow-water model and by (b) the NCAR reference spectral model at T106. Contour line spacing is 4 m s^{-1}.

more, simple arithmetic averaging onto the edge is used to compute η_l, $\overline{h}_l$.

The value of the tangential velocity component at time step $n + 1$ can be recovered by deriving the analog of Eq. (15) for the tangential velocity component and performing again a semi-implicit time discretization. This yields

$$v_l^{n+1} = v_l^n - \Delta t \tilde{\overline{\eta}}_l^{n+\alpha} u_l^{n+\alpha} - \Delta t[\delta_\tau(g(h^{n+\alpha} + h^s) + \tilde{K}^{n+\alpha})]_l. \quad (28)$$

Here, the values v_l^n are to be determined by reconstruction of the full velocity vector at time n at the velocity node l, as discussed in section 5. Furthermore, in order to compute $\delta_\tau[g(h^{n+\alpha} + h^s) + \tilde{K}^{n+\alpha}]$, values of $h^{n+\alpha}$, $\tilde{K}^{n+\alpha}$ at the vertices of the triangular cells have to be computed. In the present preliminary implementation, this is done by simple area-weighted averaging. Substituting Eq. (28) into (26) yields

$$u_l^{n+1} = \gamma_l \mathcal{F}_l^n(u) + g\gamma_l \tilde{\overline{\eta}}_l^{n+\alpha} \alpha^2 \Delta t^2 (\delta_\tau h^{n+1})_l - g\gamma_l \alpha \Delta t (\delta_\nu h^{n+1})_l, \quad (29)$$

where

$$\mathcal{F}_l^n(u) = u_l^n + \Delta t \tilde{\overline{\eta}}_l^{n+\alpha} v_l^n - \alpha(1-\alpha)\Delta t^2 (\overline{\eta}_l^{n+\alpha})^2 u_l^n - (1-\alpha)\Delta t(\delta_\nu g h^n)_l - \Delta t(\delta_\nu g h^s)_l - \Delta t(\delta_\nu \tilde{K}^{n+\alpha})_l + \alpha(1-\alpha)\Delta t^2 \overline{\eta}_l^{n+\alpha}(\delta_\tau g h^n)_l + \alpha \Delta t^2 \overline{\eta}_l^{n+\alpha}(\delta_\tau \tilde{K}^{n+\alpha})_l \quad (30)$$

and $\gamma_l = 1/[1 + \alpha^2 \Delta t^2 (\tilde{\overline{\eta}}_l^{n+\alpha})^2]$. Substitution of (29) into (27) yields for each cell i the discrete wave equation

$$h_i^{n+1} - g\alpha^2 \Delta t^2 \operatorname{div}[\overline{h}^n \gamma(\delta_\nu h^{n+1} - \alpha \Delta t \tilde{\overline{\eta}}^{n+\alpha} \delta_\tau h^{n+1})]_i = \mathcal{F}_l^n(h), \quad (31)$$

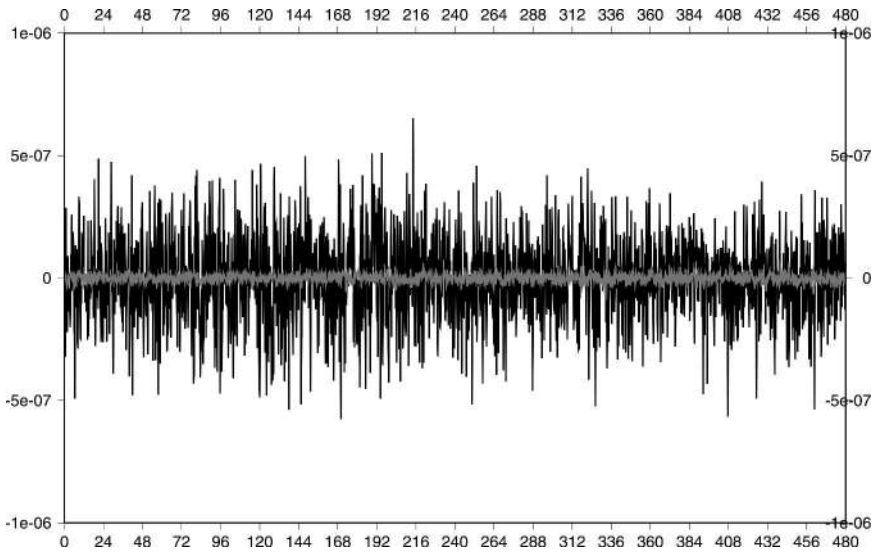

FIG. 6. Time evolution of total vorticity (black line) and total divergence (gray line) in test case 5, as computed by the semi-implicit C-grid shallow-water model.

where

$$\mathcal{F}_I^n(h) = h_i^n - (1 - \alpha)\Delta t \,\mathrm{div}(\overline{h}^n u^n)_i - \alpha\Delta t \,\mathrm{div}[\overline{h}^n \gamma \mathcal{F}^n(u)]_i.$$

The set of all Eqs. (31) for each cell i yields a linear system in the unknowns h_i^{n+1}. Its matrix is sparse and its symmetric part is positive definite and diagonally dominant. Furthermore, the asymmetric part of the matrix is multiplied by $\overline{\eta}^2\Delta t^2$, so that for typical large-scale atmospheric flows the resulting matrix is a relatively weak asymmetric perturbation of an M matrix. Finally, since time discretization of (1) and (3) must also preserve consistency with continuity, the conservation law for the tracer should be discretized in time accordingly as

$$c_i^{n+1}h_i^{n+1} = c_i^n h_i^n - \Delta t \,\mathrm{div}(\overline{c}\overline{h}^n u^{n+\alpha})_i. \qquad (32)$$

8. Numerical tests

To demonstrate that the proposed C-grid variable arrangement can be effectively implemented to achieve a useful discretization of the shallow-water equations,

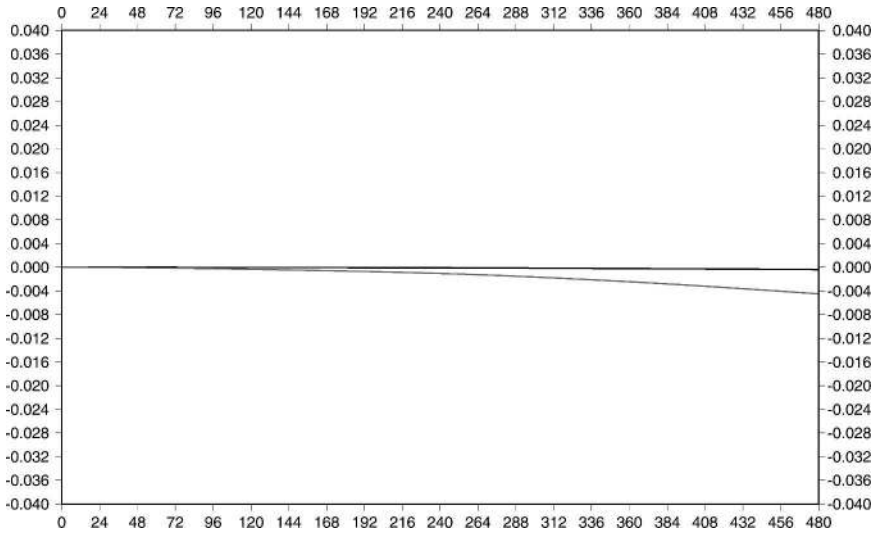

FIG. 7. Relative changes of total energy (black line) and total potential enstrophy (gray line) in test case 5, as computed by the semi-implicit C-grid shallow-water model.

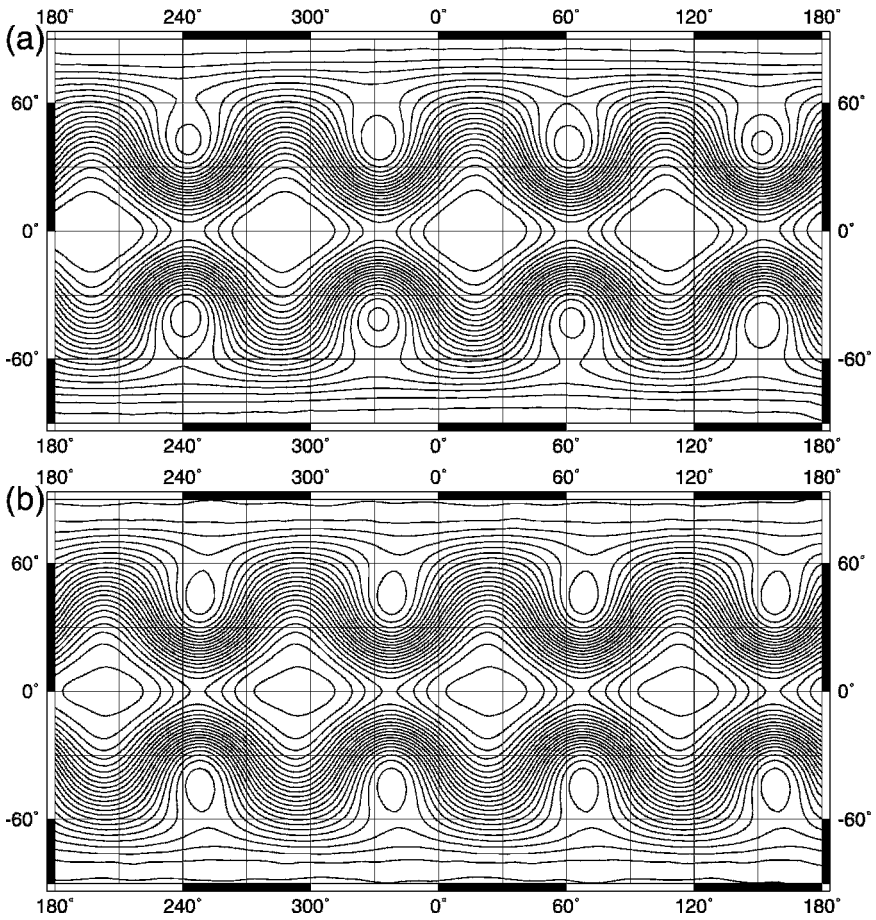

FIG. 8. Geopotential height at day 10 in test case 6, as computed by (a) the C-grid shallow-water model and by (b) the NCAR reference spectral model at T106. Contour line spacing is 100 m.

the semi-implicit time discretization described in section 7 was used to perform various numerical experiments. As is customary in the development of these types of models, the standard shallow-water test suite in Williamson et al. (1992) has been considered as a benchmark. This test suite comprises a number of idealized tests that are representative of some main features of large-scale atmospheric motion. The aim of the numerical experiments presented here is to assess whether the proposed method is reproducing correctly these basic features of atmospheric flows. Complete quantitative evaluation of an improved implementation is currently being carried out. Since a complete normal mode or stability analysis has not yet been carried out, no explicit diffusion was employed in our numerical experiments, in order to avoid suppressing possible spurious modes or instabilities. The only intrinsic damping mechanism was provided by the off-centering of the time discretization, as it is often the case in two-time-level semi-implicit schemes (see, e.g., Bonaventura 2000). The implicitness parameter α was taken to be equal to 0.6 in all the tests performed. This yields an inherently dissipative scheme, which is often used without adding further explicit diffusion.

Test case 3 of the standard shallow-water suite (Williamson et al. 1992) consists of a steady-state, zonal geostrophic flow with a narrow jet at midlatitudes. For this test case, an analytic solution is available, so that approximate convergence rates can be computed by applying the numerical method at different resolutions. The value of the relative error in various norms is displayed in Table 3, as obtained at day 10 with different spatial resolutions and with time step $dt = 900$ s. It can be observed that the estimated convergence rates are generally in the range [1.5, 1.8], as a result of the slight off-centering of the grid and of the time discretization. In this, as well as in all other tests discussed below, the relative changes in the total mass are of the order 10^{-9} and also do not display any trend in longer-term integrations. It should be remarked that, for semi-implicit

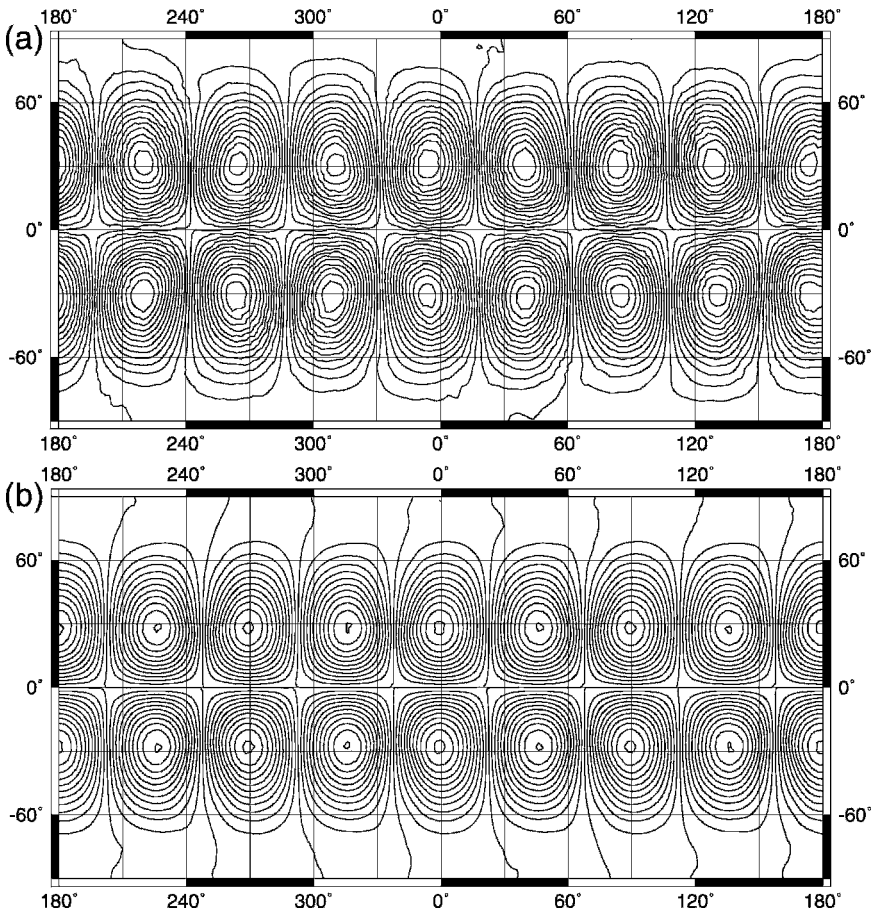

FIG. 9. Meridional velocity at day 10 in test case 6, as computed by (a) the C-grid shallow-water model and by (b) the NCAR reference spectral model at T106. Contour line spacing is 8 m s^{-1}.

models using iterative solvers for the implicit step, the precision of mass conservation is actually limited to the tolerance employed in the stopping criterion used by the iterative solvers.

In test case 5 of Williamson et al. (1992) the initial datum consists of a zonal flow impinging on an isolated mountain of conical shape. The imbalance in the initial datum leads to the development of a wave that propagates all around the globe. This test is relevant to understand the response of the numerical model to orographic forcing and it has been a common benchmark since the development of the first spectral models (see, e.g., Gill 1982). Plots of geopotential height and of the meridional velocity component at simulation day 15 are shown in Figs. 4 and 5, respectively. They were computed by the previously described shallow-water model and by a revised version of the reference spectral model of the National Center for Atmospheric Research (NCAR) described in Jakob-Chien et al. (1995), respectively. The spectral resolution for the reference model was T106. The resolution for the C-grid shallow-water model was approximately 1° and the time step was Δt = 900 s. It can be observed that all the main features of the flow are correctly reproduced. The evolution of the global integrals of vorticity and divergence over 20 simulation days is shown in Fig. 6. These integrals are zero at the initial time and their values should remain constant for the whole integration. It can be observed that the values of these global invariants computed by the model are consistently small and do not display any spurious trend. For the same test, the relative changes of total energy and total potential enstrophy over 20 simulation days are also shown in Fig. 7.

In test case 6 of Williamson et al. (1992) the initial datum consists of a Rossby–Haurwitz wave of wavenumber 4. This type of wave is an analytic solution for the barotropic vorticity equation and has also been widely used to test shallow-water models, since the analysis in Hoskins (1973) supported the view that wavenumber 4 is stable also as a solution of the shal-

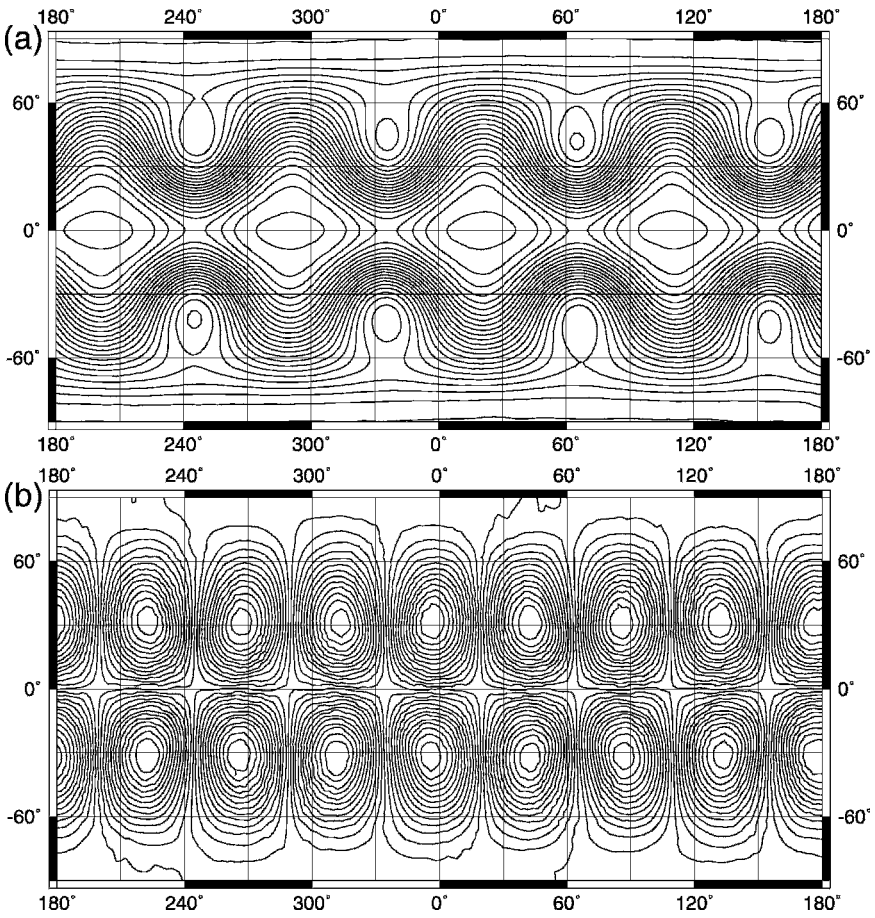

FIG. 10. (a) Geopotential height and (b) meridional velocity at day 10 in test case 6, as computed by the C-grid shallow-water model with time step $\Delta t = 450$ s. Contour lines as in the previous plots.

low-water equations. However, some recent work presented in Thuburn and Li (2000) has shown that the Rossby–Haurwitz wave of test 6 is actually unstable as a solution of the shallow-water equations, since small random perturbations in the initial datum result in long-term disruption of the wavenumber 4 pattern. This was shown to be the case for a wide range of numerical models, including spectral transform models. For all models using grids that are not symmetrical across the equator, the disruption is actually faster, but this should not be interpreted as a shortcoming of the model. Therefore, the usefulness of the Rossby–Haurwitz wave of wavenumber 4 as a benchmark for the solution of the shallow-water initial value problem is limited to time ranges shorter than those sometimes considered in the literature. On the other hand, global conservation properties must still hold on longer time intervals also for this case.

Plots of geopotential height and of the meridional velocity component at simulation day 10 are shown in Figs. 8 and 9, respectively. The resolution for the C-grid shallow-water model was approximately 1° and the time step was $\Delta t = 900$ s. It can be observed that all the main features of the flow are correctly reproduced. A slight phase delay is apparent in the solutions produced by the proposed numerical model. This can be attributed to the first-order-accurate time discretization of the nonlinear momentum terms, considering that the time step is quite large for the very strong winds present in this test case. Plots of geopotential height and of the meridional velocity component at simulation day 10 are computed with the shorter time step $\Delta t = 450$ s. are shown in Fig. 10. It can be observed that the phase delay is sensibly reduced. The evolution of the global integrals of vorticity and divergence over 20 simulation days is shown in Fig. 11. These integrals are zero at the initial time and their values should remain constant for the whole integration. It can be observed that the values of these global invariants computed by the model are consistently small and do not display any spurious

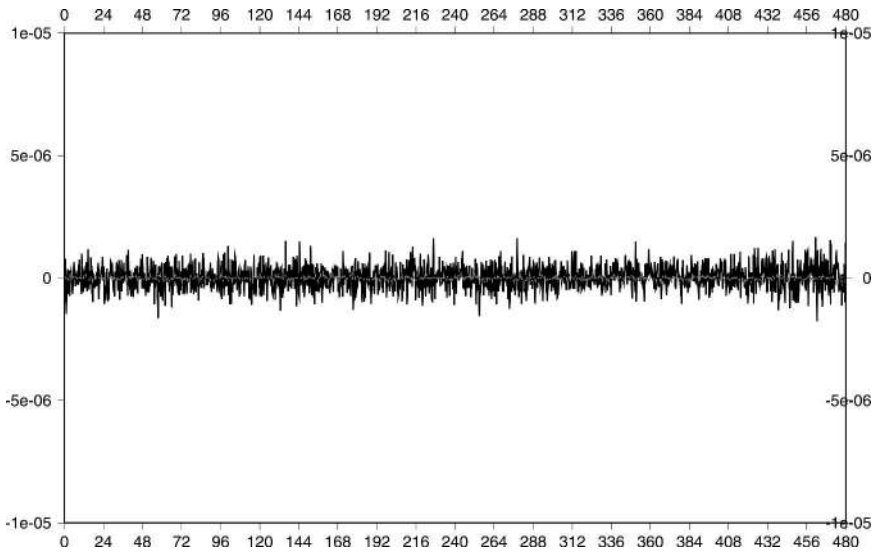

FIG. 11. Time evolution of total vorticity (black line) and total divergence (gray line) in test case 6, as computed by the semi-implicit C-grid shallow-water model.

trend. For the same test, the relative changes of total energy and total potential enstrophy over 20 simulation days are also shown in Fig. 12, as computed on a geodesic grid of resolution approximately 1° and with a time step $\Delta t = 225$ s.

Although the tests proposed in Williamson et al. (1992) provide an appropriate benchmark for the solution of the initial value problem for the shallow-water equations, they are not sufficient to test the discretization response to noisy and unbalanced initial data. Furthermore, they are not really adequate to assess whether the discrete model displays a long-term behavior that is at least qualitatively consistent with some well-known properties of two-dimensional large-scale rotating flows. The continuous shallow-water system is known to display an energy cascade toward larger spatial scales (see, e.g., Pedlosky 1987; Salmon 1998), which is directly related to an enstrophy cascade to smaller spatial scales. The energy cascade only takes place if enstrophy is removed at the grid scale. Furthermore, dimensional analysis indicates that the expected energy spectrum is steeper than the enstrophy spectrum (the theoretical

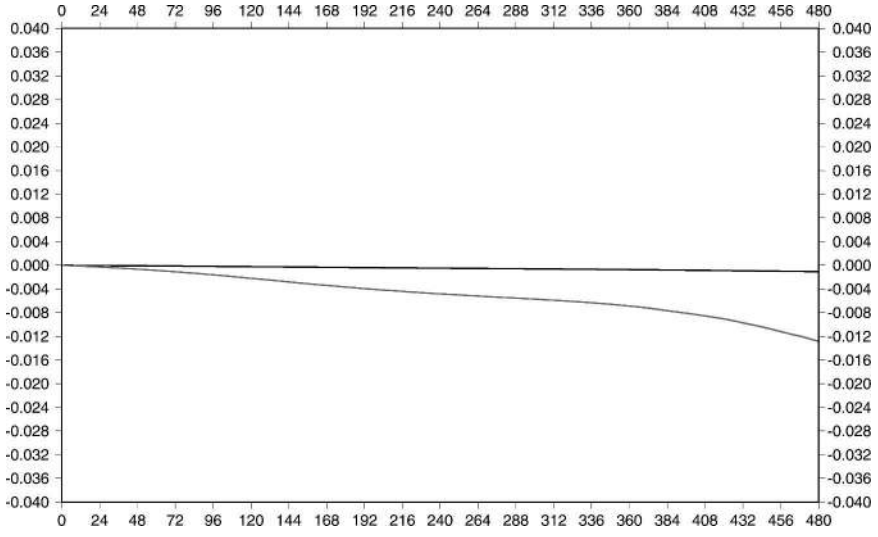

FIG. 12. Relative changes of total energy (black line) and total potential enstrophy (gray line) in test case 6, as computed by the semi-implicit C-grid shallow-water model.

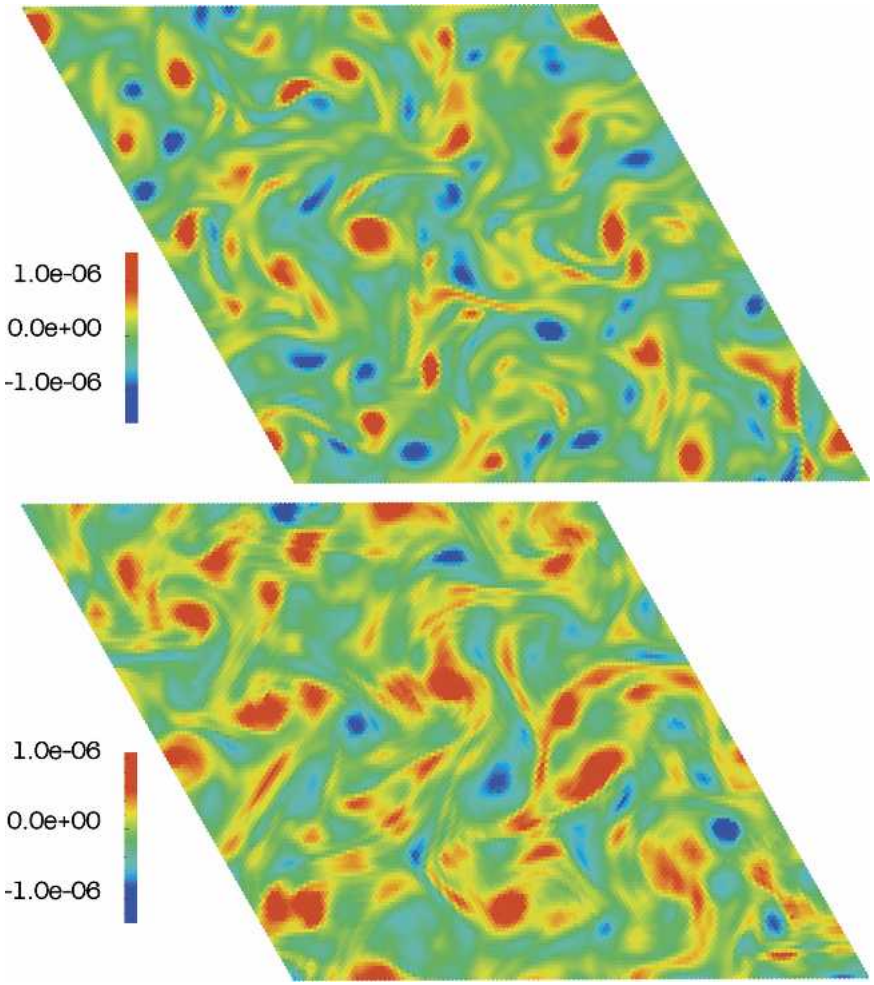

FIG. 13. Relative vorticity at day 1000 in the random initial datum test, as computed by the (top) C-grid and (bottom) ZM-grid shallow-water models.

values are k^{-3} and k^{-1}, respectively, as a function of the wavenumber k). For a more thorough discussion of recent progress in understanding two-dimensional (decaying) turbulence, see, for example, Bracco et al. (2000) and Smith et al. (2002).

Shallow-water decaying turbulence tests have been proposed in Ringler and Randall (2002), as a way to provide an evaluation of numerical model behavior in this perspective. Such an evaluation is relevant to understand whether given numerical techniques are suitable for long-range, climate-type simulations and has a rather different aim than the evaluation of the accuracy in the computation of the solutions to benchmark initial value problems. More precisely, the purpose of the tests proposed in Ringler and Randall (2002) was to assess whether, provided that suitable dissipation mechanisms are present, the discrete system response to an unbalanced, disordered initial state is analogous to the response of the continuous system. In numerical models, the enstrophy removal mechanism is usually modeled by hyperdiffusion operators, which will then have to be added to the numerical method to start the energy cascade. However, numerical diffusion is sometimes also necessary for other, purely numerical reasons, that is, to stabilize the numerical methods employed. Thus, another important test is to check whether these dissipative terms are indeed only a model for subgrid processes or whether the numerical method becomes unstable in absence of these terms. This was achieved in Ringler and Randall (2002) by switching off explicit numerical diffusion and analyzing the discrete model behavior also in this case.

To perform a clear comparison with the results of the energy- and enstrophy-preserving scheme described in Ringler and Randall (2002), the potential-enstrophy-conserving spatial discretization was coupled to third-

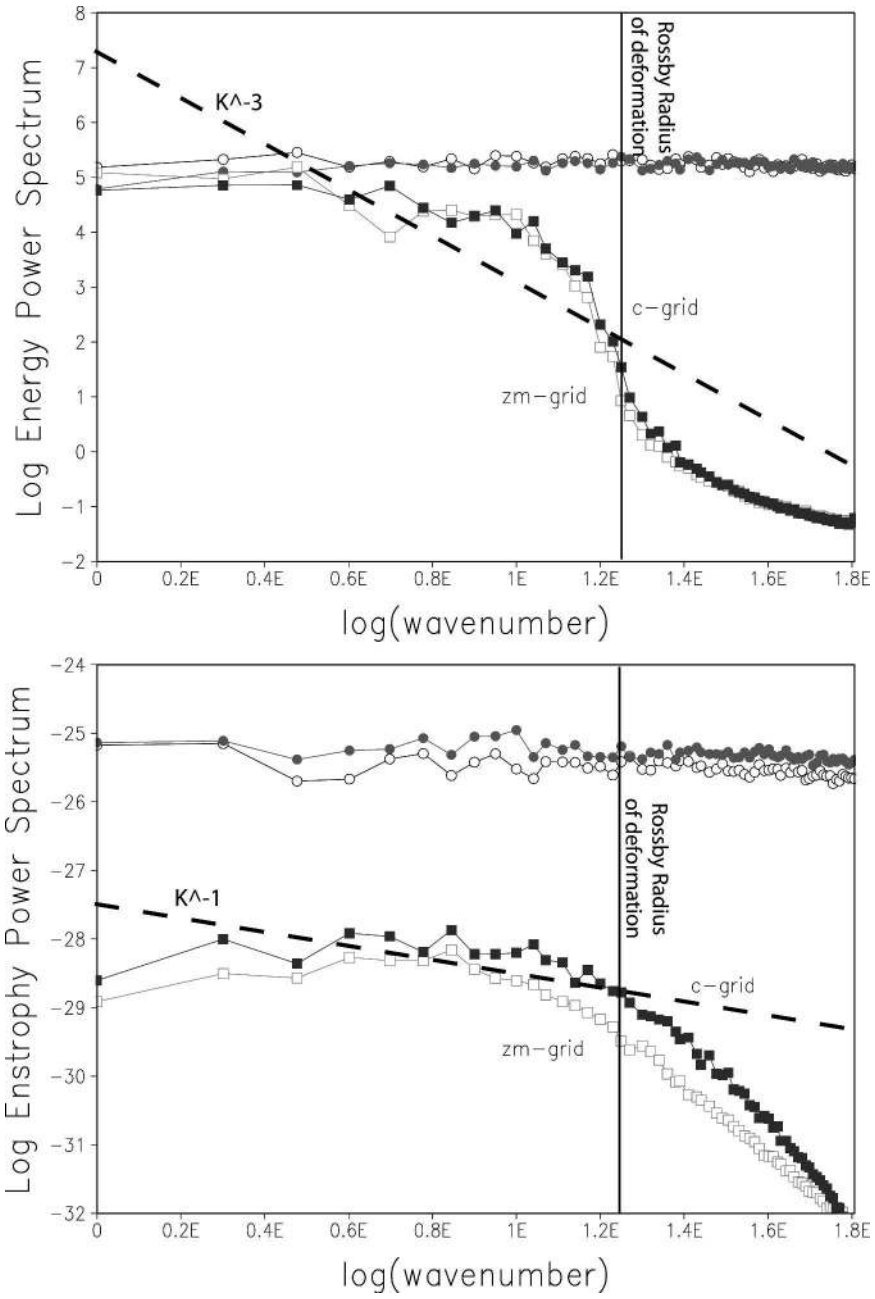

FIG. 14. (top) Total energy power spectrum and (bottom) enstrophy power spectrum at day 1000 in the random initial datum test, as computed by the C-grid and ZM-grid shallow-water models.

order Adams–Bashforth explicit time discretization, and the resulting scheme was implemented for a grid composed of equilateral triangles on a periodic f plane. The f plane was discretized setting $\lambda_l = 100$ km for all edges and assuming $f = 1 \times 10^{-4}\ \mathrm{s}^{-1}$. Both the C-grid model and the ZM-grid model of Ringler and Randall (2002) were initialized with a white noise velocity field ranging from -0.50 to $+0.50\ \mathrm{m\ s}^{-1}$ and a white noise height field ranging from 350 to 450 m. Qualitatively, the initial conditions are equivalent to those given in Ringler and Randall (2002, their Fig. 7a). Enstrophy dissipation mechanisms were simulated in the C-grid and ZM-grid models by a ∇^6 diffusion on the velocity field. Hyperdiffusion coefficients were given values of 5×10^{21} and $5 \times 10^{18}\ \mathrm{m}^6\ \mathrm{s}^{-1}$, respectively. The different values were chosen to produce in each model similar

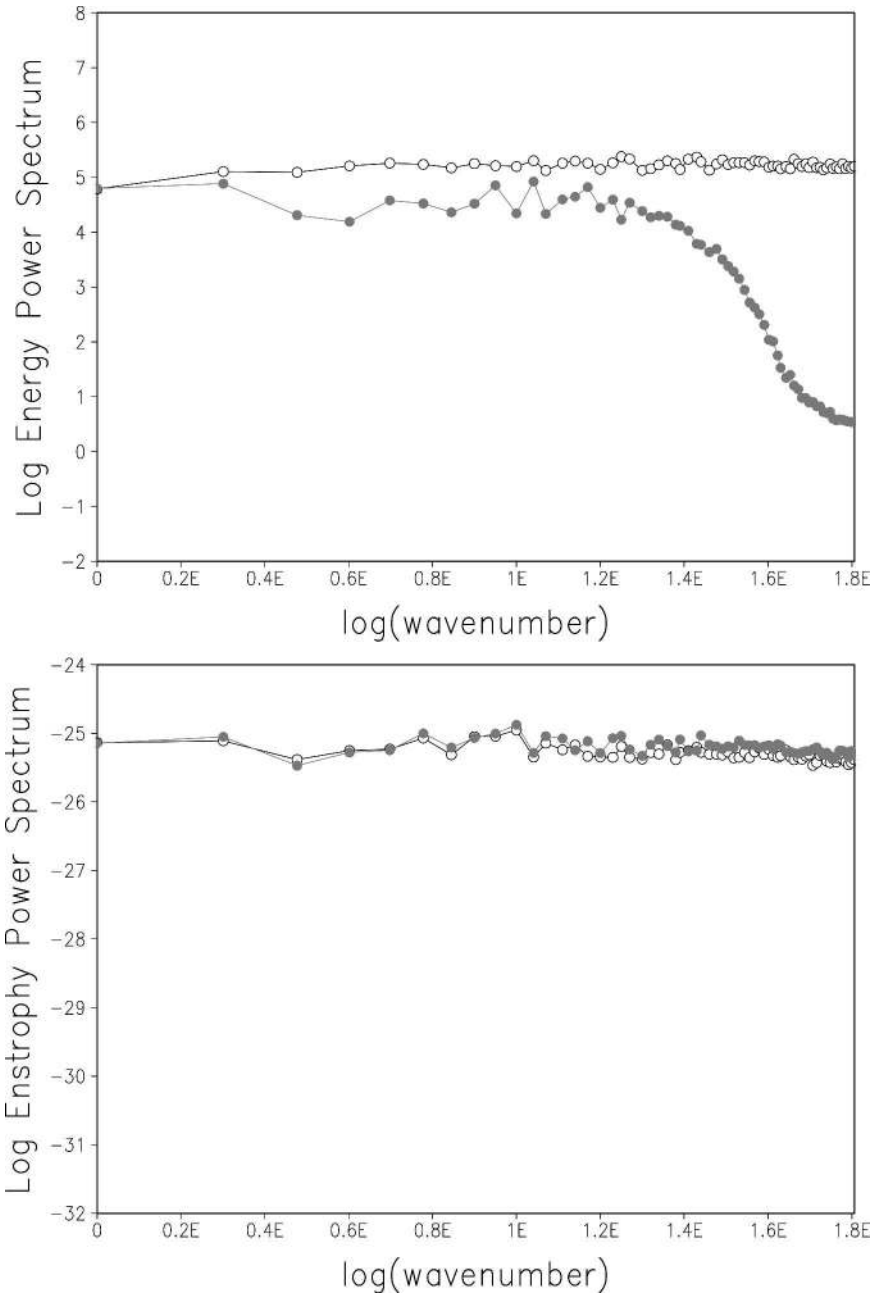

FIG. 15. (top) Total energy power spectrum and (bottom) enstrophy power spectrum at day 40 in the random initial datum test without artificial viscosity, as computed by the C-grid model.

rates of decay at day 1000, considering that, due to the use of different control volumes and velocity points, the effective resolution of the two models is not exactly the same.

Figure 13 shows the relative vorticity field at day 1000 of the C-grid simulation and the ZM-grid simulation. The color bar range differs between the plots, but each plot shows the locations of data ranging from -10^{-6} to 10^{-6}. Both models produce reasonable-looking relative vorticity fields. The fields are characterized by coherent and localized regions of positive and negative vorticity, intertwined by smaller-scale filament structures.

Figure 14 shows the power spectra of total energy and enstrophy from day 0 and day 1000. The closed symbols denote C-grid data, while the open symbols

denote ZM-grid data. The white noise initial conditions are apparent in both the energy and enstrophy fields. As in Ringler and Randall (2002), the spectra of energy exhibit steeper slopes than the spectra of enstrophy. It is to be remarked that entirely analogous results would be obtained if, instead of Eq. (20), the simpler arithmetic averaging were used to compute $\overline{\eta}_l$. The shape of the energy spectrum, including the slope through the inertial range, is also in good agreement with other high Reynolds number, decaying two-dimensional turbulence numerical experiments (see, e.g., Fig. 3 in Bracco et al. 2000).

This type of test was also repeated for the C-grid model after setting the ∇^6 diffusion coefficients to zero. The power spectra of total energy and enstrophy at day 40 are shown in Fig. 15. On one hand, the lack of energy conservation is apparent. However, it can be observed that the potential enstrophy spectrum is essentially unchanged and that no enstrophy buildup takes place at the smallest scales. In spite of the absence of explicit numerical diffusion and of the very noisy initial datum, no numerical instability arises and the discrete shallow-water system exhibits the same behavior as the continuous one, in that no enstrophy cascade is started by purely numerical reasons.

9. Conclusions

The properties of spatial discretizations of the shallow-water equations employing C-type staggering on Delaunay triangulations of the sphere have been analyzed. Potential-enstrophy- and energy-conserving schemes have been introduced on these triangular grids, along the lines of Sadourny (1975). Various other properties of these schemes have also been proved with the help of the results in Nicolaides (1992). The semi-implicit discretization introduced in Bonaventura (2003) has been employed to show that these numerical schemes reproduce correctly the main features of large-scale atmospheric flows. Furthermore, the power spectra for energy and potential enstrophy obtained in long model integrations display a qualitative behavior similar to that predicted by the decaying turbulence theory for the continuous system. These results motivate the conclusion that the present discretization approach can provide a sound basis for the development of unified numerical models for weather forecasting and climate simulation.

Acknowledgments. This work has been carried out in the context of the ICON project for the development of a new nonhydrostatic dynamical core at Max-Planck-Institut für Meteorologie, Hamburg, and Deutscher Wetterdienst. The continuous support of Erich Roeckner, Detlev Majewski, and the whole ICON development team is gratefully acknowledged, with special thanks to Marco Giorgetta and Thomas Heinze for a careful reading of the manuscript and to Luis Kornblueh for helping with the grid generator and spectral reference model. The insights and useful discussions provided by David Randall throughout this work are gratefully acknowledged. We would also like to thank the two anonymous reviewers for their useful and constructive comments, which helped to improve the previous version of the paper. One of us (TR) was also supported under DOE Cooperative Agreement DE-FC02-10ER63163.

APPENDIX A

Derivation of the Potential-Enstrophy-Conserving C-Grid Discretization

To prove that the scheme specified by Eqs. (14) and (15) conserves potential enstrophy, the advective form of the tracer equation is derived first. More precisely, from Eqs. (18) and (19) one obtains

$$h_v \frac{\partial q_v}{\partial t} = \frac{\partial (q_v h_v)}{\partial t} - q_v \frac{\partial h_v}{\partial t} = -\mathrm{div}(\overline{q}\overline{h}\mathbf{v})_v + q_v \,\mathrm{div}(\overline{h}\mathbf{v})_v. \tag{A1}$$

Potential enstrophy is defined as η^2/h, so that the time derivative of its discrete counterpart at a vorticity point is given by

$$\begin{aligned}\frac{\partial q_v^2 h_v}{\partial t} &= q_v^2 \frac{\partial h_v}{\partial t} + 2 q_v h_v \frac{\partial q_v}{\partial t}, \\ &= -q_v^2 \,\mathrm{div}(\overline{h}\mathbf{v})_v - 2 q_v \,\mathrm{div}(\overline{q}\overline{h}\mathbf{v})_v + 2 q_v^2 \,\mathrm{div}(\overline{h}\mathbf{v})_v, \\ &= q_v^2 \,\mathrm{div}(\overline{h}\mathbf{v})_v - 2 q_v \,\mathrm{div}(\overline{q}\overline{h}\mathbf{v})_v, \\ &= -\frac{1}{A_v} \sum_{l \in \mathcal{E}(v)} \overline{h}_l v_l (2 q_v \overline{q}_l - q_v^2) \mathbf{T}_l \cdot \mathbf{n}_{v,l} \delta_l. \end{aligned} \tag{A2}$$

In order for Eq. (A2) to be the discretization of a conservation law on a generic dual cell, the quantity in square brackets must depend only on the edge l and must be the same for the two dual cells that have edge l in common. More precisely, for potential enstrophy conservation to hold, one must require

$$2 q_{v(l,1)} \overline{q}_l - q_{v(l,1)}^2 = 2 q_{v(l,2)} \overline{q}_l - q_{v(l,2)}^2 \tag{A3}$$

for each edge l, which is equivalent to the requirement that

$$\overline{q}_l = \frac{q_{v(l,1)} + q_{v(l,2)}}{2}. \quad \text{(A4)}$$

This implies in turn that the numerical scheme given by Eqs. (14) and (15) will conserve potential enstrophy if one defines

$$\overline{\eta}_l = \frac{\overline{h}_l}{2}\left[\frac{\eta_{v(l,1)}}{h_{v(l,1)}} + \frac{\eta_{v(l,2)}}{h_{v(l,2)}}\right]. \quad \text{(A5)}$$

APPENDIX B

Derivation of the Energy-Conserving C-Grid Discretization

To obtain conservation of total energy, the rotation term has to be computed locally and then averaged to the adjacent velocity points. The discretization of the continuity equation is unchanged, while the discrete momentum equation is given by

$$\frac{\partial u_l}{\partial t} = \sum_{l' \in \mathcal{E}(l)} \beta_{l,l'} u_{l'} \overline{h}_{l'} - \delta_v[g(h + h^s) + K]_l. \quad \text{(B1)}$$

Here, only the discretization of the rotation term has been changed and one defines

$$\beta_{l,l'} = q_{i(l,l')} \frac{\lambda_{l'}\delta_{l'}}{\lambda_{l'}\delta_{l'} + \lambda_l\delta_l} \mathbf{T}_l \cdot \mathbf{N}_{l'}, \quad \text{(B2)}$$

where $i(l, l')$ denotes the triangular cell which has both l, l' as edges and the potential vorticity value at that cell is recovered by linear interpolation.

The time derivative of E can be expanded as follows:

$$\begin{aligned}\frac{\partial E}{\partial t} &= \sum_i A_i \left[g(h_i + h_i^s)\frac{\partial h_i}{\partial t} + K_i \frac{\partial h_i}{\partial t} + h_i \frac{\partial K_i}{\partial t}\right], \\ &= -\sum_i A_i g(h_i + h_i^s)\,\mathrm{div}(\overline{h}u)_i \\ &\quad - \sum_i A_i K_i \,\mathrm{div}(\overline{h}u)_i + \sum_i A_i h_i \frac{\partial K_i}{\partial t}. \quad \text{(B3)}\end{aligned}$$

Using now the integration-by-parts formula

$$\sum_i A_i \phi_i \,\mathrm{div}(g)_i = -\sum \delta_v \phi_l g_l \lambda_l \delta_l$$

(see section 4), one obtains

$$\begin{aligned}\frac{\partial E}{\partial t} &= \sum_l \overline{h}_l u_l \delta_v[g(h + h^s) + K]_l \lambda_l \delta_l \\ &\quad + \sum_i A_i h_i \sum_{l \in \mathcal{E}(i)} R_{i,l} u_l \sum_{l' \in \mathcal{E}(l)} \beta_{l,l'} u_{l'} \overline{h}_{l'} \\ &\quad - \sum_i A_i h_i \sum_{l \in \mathcal{E}(i)} R_{i,l} u_l \delta_v[g(h + h^s) + K]_l. \quad \text{(B4)}\end{aligned}$$

Observe now that, for a generic c_l,

$$\sum_i A_i h_i \sum_{l \in \mathcal{E}(i)} R_{i,l} c_l = \sum_l c_l [R_{i(l,1),l} A_{i(l,1)} h_{i(l,1)} + R_{i(l,2),l} A_{i(l,2)} h_{i(l,1)}]. \quad \text{(B5)}$$

This implies that the first and the last term in the previous sum will cancel, provided that

$$\overline{h}_l \lambda_l \delta_l = R_{i(l,1),l} A_{i(l,1)} h_{i(l,1)} + R_{i(l,2),l} A_{i(l,2)} h_{i(l,1)}.$$

This holds if one chooses, for example, $\overline{h}_l = (h_{i(l,1)} + h_{i(l,2)})/2$ and $R_{i,l} = \lambda_l \delta_l / (2A_i)$. Using again (B5), the second term can be rewritten as

$$\sum_l \lambda_l \delta_l u_l \overline{h}_l \sum_{l' \in \mathcal{E}(l)} u_{l'} \overline{h}_{l'} q_{i(l,l')} \frac{\lambda_{l'}\delta_{l'}}{\lambda_{l'}\delta_{l'} + \lambda_l \delta_l} \mathbf{T}_l \cdot \mathbf{N}_{l'}.$$

Rearranging the sum, one can see that each pair of edges (l, l') that have a common vertex contributes with two terms, the sum of which is zero because of the fact that $\mathbf{T}_l \cdot \mathbf{N}_{l'} = -\mathbf{T}_{l'} \cdot \mathbf{N}_l$. Thus, the C-grid discretization given by Eqs. (14) and (B1) conserves total energy. Furthermore, if $\overline{\eta}_l = 0$ it can be checked directly that the proof also holds for the potential-enstrophy-conserving method given by Eqs. (14) and (15).

REFERENCES

Almgren, A., J. Bell, P. Colella, L. Howell, and M. Welcome, 1998: A conservative adaptive projection method for the variable density incompressible Navier–Stokes equations. *J. Comput. Phys.,* **142,** 1–46.

Arakawa, A., and V. Lamb, 1977: Computational design of the basic dynamical process of the UCLA GCM. *Methods in Computational Physics,* J. Chang, Ed., Academic Press, 173–265.

——, and ——, 1981: A potential enstrophy and energy conserving scheme for the shallow water equations. *Mon. Wea. Rev.,* **109,** 18–36.

Augenbaum, J., and C. Peskin, 1985: On the construction of the Voronoi mesh on the sphere. *J. Comput. Phys.,* **59,** 177–192.

Baumgardner, J., and P. Frederickson, 1985: Icosahedral discretization of the two-sphere. *SIAM J. Sci. Comput.,* **22,** 1107–1115.

Berger, M., and P. Colella, 1989: Local adaptive grid refinement for shock hydrodynamics. *J. Comput. Phys.,* **82,** 64–84.

Bonaventura, L., 2000: A semi-implicit, semi-Lagrangian scheme using the height coordinate for a nonhydrostatic and fully elastic model of atmospheric flows. *J. Comput. Phys.,* **158,** 186–213.

——, 2003: Development of the ICON dynamical core: Modelling strategies and preliminary results. *Proc. ECMWF/SPARC Workshop on Modelling and Assimilation for the Stratosphere and Tropopause,* Reading, United Kingdom, ECMWF, 197–214.

——, and G. Rosatti, 2002: A cascadic conjugate gradient algorithm for mass conservative, semi-implicit discretization of the shallow water equations on locally refined structured grids. *Int. J. Numer. Methods Fluids,* **40,** 217–230.

Bracco, A., J. McWilliams, G. Murante, A. Provenzale, and J. Weiss, 2000: Revisiting freely decaying two-dimensional turbulence at millennial resolution. *Phys. Fluids,* **12,** 2931–2941.

Casulli, V., and P. Zanolli, 1998: A three-dimensional semi-implicit algorithm for environmental flows on unstructured grids. *Proceedings of Numerical Methods for Fluid Dynamics VI,* M. J. Baines, Ed., ICFD Oxford University Computing Laboratory, 57–70.

——, and R. Walters, 2000: An unstructured grid, three-dimensional model based on the shallow water equations. *Int. J. Numer. Methods Fluids,* **32,** 331–348.

Chorin, A., and J. Marsden, 1993: *A Mathematical Introduction to Fluid Mechanics.* 3d ed. Springer.

Dukowicz, J., 1995: Mesh effects for Rossby waves. *J. Comput. Phys.,* **119,** 188–194.

Gavrilov, M., 2004: On nonstaggered rectangular grids using streamfunction and velocity potential or vorticity and divergence. *Mon. Wea. Rev.,* **132,** 1518–1521.

Gill, A., 1982: *Atmosphere–Ocean Dynamics.* Academic Press, 662 pp.

Giraldo, F. X., 2000: Lagrange–Galerkin methods on spherical geodesic grids: The shallow water equations. *J. Comput. Phys.,* **160,** 336–368.

Girault, V., and P. Raviart, 1986: *Finite Element Methods for the Navier–Stokes Equations.* Lecture Notes in Mathematics, Springer-Verlag.

Gross, E., L. Bonaventura, and G. Rosatti, 2002: Consistency with continuity in conservative advection schemes for free-surface models. *Int. J. Numer. Methods Fluids,* **38,** 307–327.

Harlow, F., and J. Welch, 1965: Numerical calculation of time dependent viscous incompressible flow. *Phys. Fluids,* **8,** 2182–2189.

Heikes, R., and D. Randall, 1995a: Numerical integration of the shallow-water equations on a twisted icosahedral grid. Part I: Basic design and results of tests. *Mon. Wea. Rev.,* **123,** 1862–1880.

——, and ——, 1995b: Numerical integration of the shallow-water equations on a twisted icosahedral grid. Part II: A detailed description of the grid and an analysis of numerical accuracy. *Mon. Wea. Rev.,* **123,** 1881–1887.

Hermeline, F., 1993: Two coupled particle-finite volume methods using Delaunay–Voronoi meshes for the approximation of Vlasov–Poisson and Vlasov–Maxwell equations. *J. Comput. Phys.,* **106,** 1–18.

Hoskins, B., 1973: Stability of the Rossby–Haurwitz wave. *Quart. J. Roy. Meteor. Soc.,* **99,** 723–745.

Jakob-Chien, R., J. Hack, and D. Williamson, 1995: Spectral transform solutions to the shallow water test set. *J. Comput. Phys.,* **119,** 164–187.

Janjic, Z., 1984: Nonlinear advection schemes and energy cascade on semi-staggered grids. *Mon. Wea. Rev.,* **111,** 1234–1245.

Jöckel, P., R. von Kuhlmann, M. Lawrence, B. Steil, C. Brenninkmeijer, P. Crutzen, P. Rasch, and B. Eaton, 2001: On a fundamental problem in implementing flux-form advection schemes for tracer transport in 3-dimensional general circulation and chemistry transport models. *Quart. J. Roy. Meteor. Soc.,* **127,** 1035–1052.

Le Roux, D. L., A. Staniforth, and C. Lin, 1998: Finite elements for shallow-water equation ocean models. *Mon. Wea. Rev.,* **126,** 1931–1951.

Leveque, R., 1996: High-resolution conservative algorithms for advection in incompressible flow. *SIAM J. Sci. Comput.,* **33,** 627–665.

Lin, S., and R. Rood, 1997: An explicit flux-form semi-Lagrangian shallow water model on the sphere. *Quart. J. Roy. Meteor. Soc.,* **123,** 2477–2498.

Liu, X., 1993: A maximum principle satisfying modification of triangle based adaptive stencils for the solution of scalar hyperbolic conservation laws. *SIAM J. Numer. Anal.,* **30,** 701–716.

Majewski, D., and Coauthors, 2002: The operational global icosahedral–hexagonal gridpoint model GME: Description and high-resolution tests. *Mon. Wea. Rev.,* **130,** 319–338.

Massey, W., 1977: *Algebraic Topology: An Introduction.* Springer Verlag, 261 pp.

Mesinger, F., 1981: Horizontal advection schemes on a staggered grid: An enstrophy and energy conserving model. *Mon. Wea. Rev.,* **109,** 467–478.

——, and A. Arakawa, 1976: *Numerical Methods Used in Atmospheric Models.* Vol. I, GARP Publication Series, No. 17, WMO.

Morton, K., and P. Roe, 2001: Vorticity preserving Lax–Wendroff type schemes for the system wave equation. *SIAM J. Sci. Comput.,* **23,** 170–192.

Ničković, S., 1994: On the use of hexagonal grids for simulation of atmospheric processes. *Contrib. Atmos. Phys.,* **67** (2), 103–107.

——, M. Gavrilov, and I. Tošić, 2002: Geostrophic adjustment on hexagonal grids. *Mon. Wea. Rev.,* **130,** 668–683.

Nicolaides, R., 1992: Direct discretization of planar div-curl problems. *SIAM J. Numer. Anal.,* **29,** 32–56.

Pedlosky, J., 1987: *Geophysical Fluid Dynamics.* Springer Verlag, 710 pp.

Quarteroni, A., and A. Valli, 1994: *Numerical Approximation of Partial Differential Equations.* Springer-Verlag.

Quiang, D., M. Gunzburger, and J. Lili, 2003: Voronoi-based finite volume methods, optimal Voronoi meshes and PDEs on the sphere. *Comput. Methods Appl. Mech. Eng.,* **192,** 3933–3957.

Randall, D., 1994: Geostrophic adjustment and the finite-difference shallow-water equations. *Mon. Wea. Rev.,* **122,** 1371–1377.

Raviart, P., and J. Thomas, 1977: A mixed finite element method for 2nd order elliptic problems. *Mathematical Aspects of Finite Element Methods,* I. Galligani and E. Magenes, Eds., Lecture Notes in Mathematics, Springer-Verlag, 292–315.

Rebay, S., 1993: Efficient unstructured mesh generation by means of Delaunay triangulation and Bowyer–Watson algorithm. *J. Comput. Phys.,* **106,** 125–138.

Ringler, T., and D. Randall, 2002: A potential enstrophy and energy conserving numerical scheme for solution of the shallow-water equations on a geodesic grid. *Mon. Wea. Rev.,* **130,** 1397–1410.

——, R. Heikes, and D. Randall, 2000: Modeling the atmospheric general circulation using a spherical geodesic grid: A new class of dynamical cores. *Mon. Wea. Rev.,* **128,** 2471–2490.

Sadourny, R., 1969: Numerical integration of the primitive equations on a spherical grid with hexagonal cells. *Proc. WMO/IUGG NWP Symp.,* Tokyo, Japan, Japan Meteorological Agency, 45–52.

——, 1975: The dynamics of finite-difference models of the shallow-water equations. *J. Atmos. Sci.,* **32,** 680–689.

——, and P. Morel, 1969: A finite-difference approximation of the primitive equations for a hexagonal grid on a plane. *Mon. Wea. Rev.,* **97,** 439–445.

——, A. Arakawa, and Y. Mintz, 1968: Integration of the nondivergent barotropic vorticity equation with an icosahedral-hexagonal grid for the sphere. *Mon. Wea. Rev.,* **96,** 351–356.

Salmon, R., 1998: *Lectures on Geophysical Fluid Dynamics.* Oxford University Press, 378 pp.

Schär, C., and P. Smolarkiewicz, 1996: A synchronous and iterative flux-correction formalism for coupled transport. *J. Comput. Phys.,* **128,** 101–120.

Smith, K., G. Boccaletti, C. Henning, I. Marinov, C. Tam, I. Held, and G. Vallis, 2002: Turbulent diffusion in the geostrophic inverse cascade. *J. Fluid Mech.,* **469,** 13–48.

Stuhne, G., and W. Peltier, 1999: New icosahedral grid-point discretizations of the shallow water equations on the sphere. *J. Comput. Phys.,* **148,** 23–58.

Thuburn, J., 1997: A PV-based shallow-water model on a hexagonal–icosahedral grid. *Mon. Wea. Rev.,* **125,** 2328–2347.

——, and Y. Li, 2000: Numerical simulation of Rossby–Haurwitz waves. *Tellus,* **52A,** 181–189.

Tomita, H., M. Tsugawa, M. Satoh, and K. Goto, 2001: Shallow water model on a modified icosahedral grid by using spring dynamics. *J. Comput. Phys.,* **174,** 579–613.

Williamson, D., 1968: Integration of the barotropic vorticity equation on a spherical geodesic grid. *Tellus,* **20,** 642–653.

——, 1979: Difference approximations for fluid flow on a sphere. *Numerical Methods Used in Atmospheric Models,* Vol. II, GARP Publication Series, No. 17, WMO, 53–123.

——, J. Drake, J. Hack, R. Jakob, and R. Swarztrauber, 1992: A standard test set for numerical approximations to the shallow water equations in spherical geometry. *J. Comput. Phys.,* **102,** 221–224.

Winninghoff, F., 1968: On the adjustment toward a geostrophic balance in a simple primitive equation model. Ph.D. thesis, University of California, Los Angeles.